# ENERGY LOSS CHARACTERIZATION OF THE P3 MEMS HEAT ENGINE

By

KIRSTEN ELIZABETH McNEIL

A thesis submitted in partial fulfillment of
the requirements for the degree of

MASTER OF SCIENCE IN MECHANICAL ENGINEERING

WASHINGTON STATE UNIVERSITY
School of Mechanical and Materials Engineering

August 2006

To the Faculty of Washington State University:

The members of the Committee appointed to examine the thesis of KIRSTEN ELIZABETH MCNEIL find it satisfactory and recommend that it be accepted.

_____
Chair

_____

_____

## ACKNOWLEDGMENT

I would like to thank my committee members and the other members of the MEMS team, past and present, for their consistent advice and support throughout my work on the project. A great man once said, If I have contributed anything, it is because I have stood on the shoulders of giants. I am deeply grateful for the commitment and enthusiasm of the entire group. My advisor, Dr. Cill Richards, requires special acknowledgement for her support throughout my graduate work, allowing a good balance in my coursework which directly benefited my research and understanding. I am glad to have completed the process in the way I did. My other committee members, Dr. Robert Richards and Dr. David Bahr, have each profoundly influenced my understanding and progress on my research project. Direct acknowledgement is required for Robert Gifford as well, whose research I am continuing. I have built off of his foundation. Hopefully what I contribute will be of value to the group after I am gone, and can serve as a foundation for another incoming student.

ENERGY LOSS CHARACTERIZATION OF THE P3 MEMS HEAT ENGINE


## Abstract

by Kirsten Elizabeth McNeil, M.S.
Washington State University
August 2006

Chair: Cill D. Richards

The P3 MEMS heat engine has been developed to convert waste heat into useful electrical energy. Such energy conversion devices are complex systems. Other micro engines under development around the world are facing similar challenges, but the P3 micro heat engine has a special advantage, building from the principles which govern the scale on which it is designed. The engine system has many parameters, including membrane size, cavity thickness, bubble size and initial deflection, each of which influences the operation of the system. The free vibration response of the engine has been studied to characterize each aspect of the system and determine the dominant parameters. Governing equation analysis details the relationship between the mass, stiffness and damping of each component of the system.

Two main figures of merit are currently used to study the engine system: resonant frequency and quality factor (Q). These two parameters have been extensively characterized for many different engine configurations. Trends of these figures of merit with the engine parameters have been determined. Experiments and modeling of the engine show that a higher upper membrane stiffness and lower liquid damping yield higher resonant frequency and Q.

The model of the engine as a linearly coupled oscillator yielded trends of Q with upper membrane stiffness, liquid stiffness, and liquid mass. A decrease of several orders of magnitude of the upper membrane stiffness results in a much greater change in Q than a similar variation in liquid stiffness. If the generator stiffness is increased by a factor of

100, resonance is about 4700Hz, with a Q of 70; whereas if the stiffness of the liquid was increased by a factor of 100, resonance is about 1570Hz with a Q of 23. The model reflects experimental trends seen with Q and bubble size as well. Varying the bubble size from 1 to 4mm yields Q values from 22.8 to 6.5, reflecting the trend seen experimentally of Q decreasing with increasing bubble size. Changing the liquid mass in the model yielded no significant changes in Q, showing that this parameter has little effect on the system. These trends along with details discovered through the model lead to the conclusion that the single most influential engine parameter is the liquid damping. Trends set the foundation for optimization, where engine performance can meet the resonant frequency goals while losing the least amount of energy to internal and external forms of friction and energy loss mechanisms. Experimental data and the linearly coupled oscillator model combine to facilitate optimization.

## TABLE OF CONTENTS

## LIST OF TABLES

## LIST OF FIGURES

# CHAPTER ONE
# INTRODUCTION

## *1.1 MASS-SPRING-DAMPER SYSTEMS*

The free vibration behavior of mass-spring-damper systems is well known, and can be expressed as a differential equation of the form:

$$m\ddot{x} + b\dot{x} + kx = 0 \qquad (1)$$

where m is the mass of the system, b is the damping coefficient, k is the system stiffness, and x is the deflection from the equilibrium position. This equation can be used to analyze any freely vibrating system with these mass, damping, and stiffness components. The P3 micro heat engine is one system that can be analyzed using this equation. Throughout this work, the focus will be on the key parameters of effective mass, damping, and stiffness, and how they contribute to energy loss in the system.

## *1.2 P3 BASICS*

The P3 micro heat engine is designed to capture waste heat from a variety of potential sources and convert this heat energy into electrical energy using a stackable, flexible fuel external combustion engine based on flexing piezoelectric membranes to produce a usable voltage output. This is accomplished by utilizing a two-phase fluid encapsulated between the two flexible membranes. When heat is applied to one side of the engine, onto the bottom membrane, the heat causes the liquid inside the cavity to evaporate, resulting in a cavity expansion. This expansion causes the upper membrane to flex; this upper membrane has a piezoelectric material on it which converts the strain into a charge. The charge can then be harvested for electricity. As the upper membrane cools, the liquid that had evaporated condenses and the cavity shrinks. The process repeats

itself, preferably at a frequency around the resonance of the engine as to yield the greatest output for a given input. A thermal switch was also designed to control heat into and out of the engine [1].

The three major components of the system are the piezoelectric membrane generator, the engine and the thermal switch. This work is focused only on the engine without the other components. Engine fabrication utilizes microfabrication technology based on semiconductor processing. The membranes are etched from boron-doped silicon wafers. The generator is made of several different thin film layers, each of which is necessary for device success. In this work, "the engine" refers to the two membranes sandwiched together, with or without a generator on top. A bare silicon membrane is used as the top membrane for ease of experimentation. All of the engines reported on in this work do not include the membrane generator.

In the engine cavity, the two-phase fluid is achieved by assembling the engine with the proper liquid/vapor ratio to form a bubble. Heat into the engine evaporates some of the liquid, which turns into vapor and expands the bubble, causing an impact on the upper membrane. Proper engine assembly technique can take weeks to learn. The size of the bubble and the initial deflection can be controlled during assembly to a certain extent.

To simulate external heat input to the engine, and control it exactly, a resistance heater is fabricated on the bottom membrane. This heater replaces the external heat source that would be used in application. The heater fabrication process is described in the fabrication section (Chapter 2). A DC voltage is applied to the heater during tests. This voltage is controlled by the circuitry explained in the experimentation section (Chapter 3). The specifics of engine assembly and fabrication very much influence the

operating parameters and output of the engine, and will impact the performance when the engine is combined with the two other major components, the generator and the thermal switch.

## *1.3 LITERATURE REVIEW*

Micro engines exist within a multitude of energy conversion devices. These engines follow different design approaches and criteria. To evaluate energy conversion devices, and these micro engines in particular, several figures of merit have been developed including the quality factor, efficiency and friction losses. The analysis of these figures of merit will yield better understanding of the devices as well as lead toward optimization and development of the best possible device configurations.

### *1.3.1 Micro Engines*

The P3 micro heat engine is one of several micro engines using MEMS technology currently being developed. These micro engines vary widely in their design and possible applications. The design paradigm used by the P3 group here at WSU is inherently different than all the rest. The other micro engines currently under development will be summarized here for comparison.

While possibly in a different class than the other micro engines, several groups are working on developing small-scale motors using electrostatics. Micromotors differ from the P3 micro heat engine in the basic operating principles. The P3 engine is designed to transform waste heat energy into electrical energy, and micromotors transform electrical energy into a mechanical output. The scaling laws that govern electromagnetics make it difficult, if not impossible to scale down the typical electromagnetic motor [2]. Therefore, to use MEMS technology, groups are turning to

electrostatics, which produce higher forces on small length scales [2]. One micro electrostatic motor is being developed for application to precision medical instruments. This micro motor is being developed to provide precision movement in a package smaller than 1mm square for applications in endoscopic surgery [3]. This micromotor produces about 2.5μNm of torque, which meets the requirements set forth for this medical application.

Single crystal silicon micromotors are also being developed. These are rotational motors, with rotors on the scale of 50μm. The micro motor components are fabricated by using deep boron diffusion and deep reactive ion etching to make high aspect ratio structures. A stepping motor has successfully been produced, as well as a harmonic motor and a gyro-type motor. No proposed application or power output was presented in this paper [4], but micromotors are commonly being developed for different kinds of sensors and actuators.

Rotating internal combustion engines are also under development on the micro scale. MIT is developing a micro gas turbine engine with a 4mm diameter rotor [5]. The fabrication of this micro turbine engine has presented many problems, and deep reactive ion etching and wafer bonding are used extensively to try to simplify the assembly process [6]. Their design is basically to scale down a macro-scale gas turbine engine and take advantage of materials that are better able to be used on the micro-scale, due to the high cost of manufacturing large components from materials such as SiC for macro-scale engines. They are also fabricating the components to go with the turbine, like the compressor and combustor. Simulations suggest an adiabatic efficiency of 70%, an electrical efficiency of 80% and an electrical power output of 20-40 watts [5], but none of

these have been validated physically. The idea for this micro engine is similar to the P3, in that both are producing power from engines with very small volumes. However, the P3 design paradigm is very different; it builds from the micro-scale up instead of scaling down a macro-scale existing engine design.

A piston-cylinder engine is also under development using combustion as well as MEMS fabrication [7]. This group confirms that combustion on the micro-scale is affected by the increased surface to volume ratio of the combustion chamber, causing increased heat loss through the walls. Combustion on the micro-scale has been studied for these applications. Combustion of the device and piston displacement was demonstrated, but engine performance was not. This engine will have to overcome not only heat transfer losses during operation, but also friction losses like any other combustion engine.

A micro Wankel engine is under development in several groups as well. The macro Wankel engine operates with one triangular-shaped rotor which rotates on an eccentric shaft to produce work output. A sliding seal moves the chambers to achieve a four-stroke cycle [8]. One micro Wankel engine under development operates at high speeds (17,000 rpm) and produces a significant amount of power (12 W). This micro engine is 15 x 12 x 3mm in size. To accommodate the high operating temperature, nickel and an SU-8 epoxy are chosen to fabricate the rotor and engine casing [9].

There are many actuators under development using MEMS technology as well. The P3 micro heat engine can also be used as an actuator, running at slower speeds. The cavity assembly design of the P3 for each mode of operation is basically the same, but the operating conditions are different. Another type of actuator is a comb drive actuator using electrostatic actuation is under development and has been demonstrated. This actuator

uses a large number of legs on the comb to increase the surface area and decrease the amount of applied charge needed to move the actuator. This particular system was operated at resonance to visually observe viscous damping by observing the deflection of the comb. A micro engine is theoretically produced by assembling these comb drives orthogonally with a round gear to transfer linear motion into rotational motion [10].

For a very exhaustive report on micro power generation with a focus on micro engines, see [11].

### *1.3.2 Engine Losses*

Friction in engines can account for a significant amount of work that is lost during engine operation. Since the whole aim of engines is to produce useful work, the understanding of energy losses is essential to an efficient engine design. Work can be dissipated in many different ways, each of which is important to understand. In the P3 micro heat engine, energy loss comes from three major sources: viscous dissipation, membrane stretching losses, and heat transfer losses. In a macro-scale combustion engine, the sources of energy loss are analogous. Major losses are seen from fluid transfer during expansion/compression of the working fluid in the cylinder, rubbing friction of all moving parts including the pistons, shafts, bearings, and seals, as well as work transferred to engine accessories [8]. Mechanical friction in combustion engines can be decomposed into which component contributes the most to friction, or conversely, which component converts the most power away from the useful output [8, 12, 13]. In gas turbine engines, combustion inefficiency also causes energy losses due to incomplete combustion, but these are not applicable to the P3 micro heat engine [8, 14, 15]. Combustion efficiency is

typically around 95%, so this does not represent a major difference when comparing efficiencies of the P3 micro engine and conventional combustion engines [8].

During operation of the P3 micro heat engine, the working fluid expands and contracts from the addition/expulsion of heat into/out of the cavity. When the fluid volume is increased, the movement of the fluid results in viscous dissipation, which is irreversible [16]. This is similar to expansion/compression losses in large-scale engines. Because fluid is expanded and compressed during the engine cycle, this causes some dissipation in the fluid. Viscous losses inside the moving fluid again cause a slight temperature increase and a loss of usable work.

There are no sliding parts in the P3 micro heat engine. Volume change is accomplished by the stretching of flexible membranes. Therefore, the only rubbing friction losses are analogous to internal dissipation in the membranes, which is very small and can be neglected. Internal friction is commonly reported as [17,18]

$$\frac{b}{\sqrt{km}} \qquad (2)$$

where b, k, and m are defined in Equation (1). Rubbing friction dominates in large, passenger vehicle engines [8, 12, 13]. The standard measurement of the largest fraction of motored friction mean effective pressure or friction power is accounted for by the piston ring friction, piston and connecting rod friction, valve gear power, and crankshaft friction, all adding up to the "Friction losses" [13]. "An approximate breakdown of rubbing and accessory friction is: piston assembly 50 percent; valve train 25 percent; crankshaft bearings 10 percent; accessories 15 percent" [8]. Every surface in a macro-scale engine that moves is subject to and adds to the friction in the engine because every surface area with lateral motion relative to another surface will cause friction. There are

so many sliding surfaces that accounting for all the friction components can make "the difference between a good engine design and an average engine" [8].

In a large engine, there are several accessories that also need to be driven by the engine along with the actual drive shaft, including oil/fuel pumps, air conditioner, and alternator. All of these take power away from the drive shaft, but are necessary for vehicle operation. So far, the P3 engine does not include any accessories, but eventually some engine power will need to be used for thermal switch operation, which is outside of the scope of this work.

The major possible sources of energy loss in the P3 engine are viscous losses and heat transfer losses. Fluid viscous losses were discussed above. When heat is applied to the engine, some heat goes into evaporating the liquid in the cavity, which produces the volume expansion, and some gets conducted into the bulk silicon around the membranes. Currently these heat transfer losses are being investigated in the P3 group, and preliminary results show that only about 10% of the heat input to the engine goes into evaporating the liquid. Therefore, almost all of the energy input as heat is lost through conduction to the bulk around the membrane and the membrane itself [19]. In a conventional internal combustion engine, the "heat converted into work (indicated) [is] 15-40 percent" of the total heat input, while the rest is lost to the cooling system, the exhaust or friction [15].

### *1.3.3 Efficiency*

The current P3 definition of efficiency takes into account all energy loss mechanisms [11]. Efficiency is defined as the ratio of mechanical (volumetric) work output to the electrical (heat) energy input. This definition will therefore include viscous

dissipation, heat transfer losses, and any internal (thermoelastic damping) membrane losses. When the quality factor is calculated from a ringout, however, only volumetric losses are taken into account: fluid viscous losses and membrane stretching losses. Q does not depend on input voltage (heat input), as will be shown later. Therefore, efficiency shows a more complete picture of all energy losses in the engine.

There are many ways to define the efficiency of an engine. The classical thermodynamic efficiency, $\eta_{th}$, is [20]

$$\eta_{th} = \frac{W_{net,out}}{Q_{in}} \tag{3}$$

where $W_{net,out}$ is the net work output and $Q_{in}$ is the heat input. This definition is based on the heat into a mechanical system and the work delivered. The thermal efficiency is what has been defined previously by the P3 group [11], describing how well the micro heat engine converts heat energy into mechanical work.

The mechanical efficiency is commonly reported for internal combustion engines, and focuses only on the respective power values during engine operation. Mechanical efficiency is defined as [21-24]

$$\eta_m = \frac{\dot{w}_{brake}}{\dot{w}_{indicated}} = \frac{\dot{w}_{indicated} - \dot{w}_{friction}}{\dot{w}_{indicated}} \tag{4}$$

where the brake power ($\dot{w}_{brake}$) is "the [shaft] power obtained from an engine" [23], the indicated power ($\dot{w}_{indicated}$) is the "total horsepower actually developed on the pistons in the engine" [23], and the friction power ($\dot{w}_{friction}$) is the power used to overcome friction in the engine [21]. For automotive-type spark ignition engines, the mechanical efficiency can be 55-90% for various vehicle and engine speeds [21]. The friction power, or power

lost to friction, increases approximately with the square of the speed of the engine [8,21]. Friction measured as the mean effective pressure (fmep), or work, lost in automotive engines can range from 50-200kPa, depending on engine speed [8].

The mechanical efficiency of an engine describes how much energy is lost to irreversibilities during operation. Therefore, mechanical efficiency will be compared with the percent friction in the P3 engine in section 5.9. Both of these values show losses due to mechanical effects, as opposed to heat transfer losses.

The friction in an engine depends directly on the engine operating speed, as well as the source of the friction. Friction increases as the speed increases, and the rate of increase depends on whether the friction comes from pumping losses, piston sliding losses, or auxiliaries [8, 23]. However, the P3 engine is designed to operate at a single speed, the resonant frequency of the system, and mechanical losses are primarily due to viscous damping and membrane effects.

### *1.3.4 Friction and Size of Engines*

The previously mentioned mechanical efficiency of internal combustion engines is 55-90% [21]. As rubbing friction dominates in these engines, the friction will increase with the size of the engine because the surface area increases. This would lead one to believe that small engines would have less friction, but this argument does not hold on the micro scale. When approaching length scales on the order of microns, scaling laws begin to dominate [2]. The surface to volume ratio increases, and friction has the potential to dominate in micro engines.

### *1.3.5 Quality Factor*

The quality factor Q is an important figure of merit for any vibrating structure. Q can describe how well the resonating structure vibrates at its resonant frequency specifically, compared to the other frequencies near it, i.e. how wide the bandwidth is. Q also defines the ratio of how much energy is stored to energy dissipated during each cycle of vibration. Some devices need a high Q to operate, and some are designed to operate over a larger bandwidth, yielding a lower Q value. Q can be measured using several different methods, including a spectrum analysis (forced vibration) and a free-vibration analysis or "ringout." From a spectrum analysis, the resonator is forced to vibrate at every frequency within the defined band, and the amplitude is measured. Q is found by calculating the full-width half-maximum of the spectral peak, as shown in Figure 1.

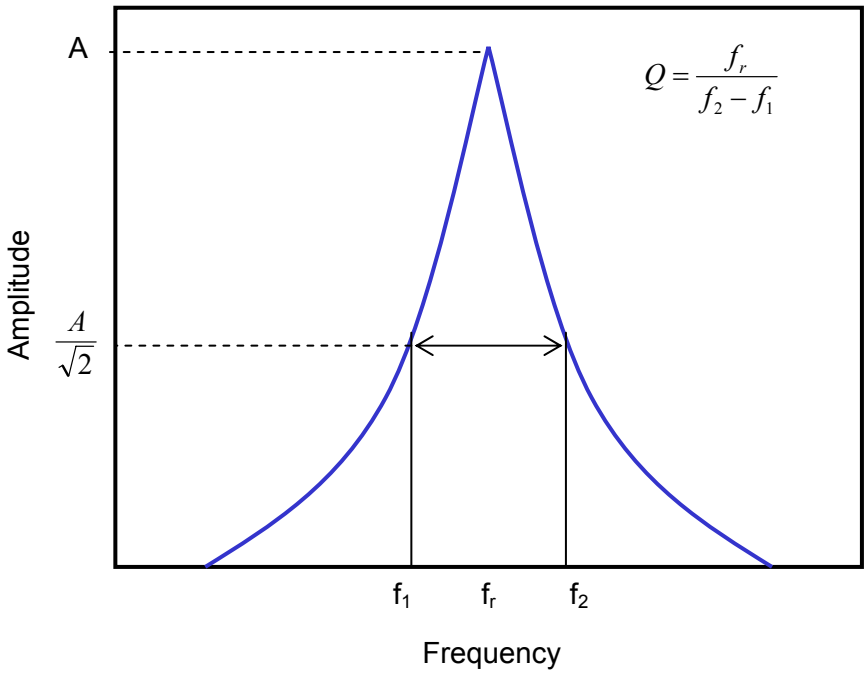


*Figure 1. Q measurement from spectral analysis: full width half maximum (forced vibration).*

The free-vibration method inputs an impulse to the resonator and measures the decaying amplitude of the resulting vibration. A ringout analysis uses the logarithmic decrement

method where the subsequent value of each amplitude peak is used to calculate the damping ratio ζ of the system using [25]

$$\varsigma = \frac{\frac{1}{n-1}\left(\ln\frac{x_1}{x_n}\right)}{\sqrt{4\pi^2 + \left[\frac{1}{n-1}\left(\ln\frac{x_1}{x_n}\right)\right]^2}} \qquad (5)$$

where n is the number of the peaks in the ringout, $x_1$ is the amplitude of the first peak of the ringout, and $x_n$ is the amplitude of the $n^{th}$ peak of the ringout, as shown in Figure 2. This method is valid for systems that can be modeled as simple mass-spring-damper systems which obey the differential equation in Equation (1).

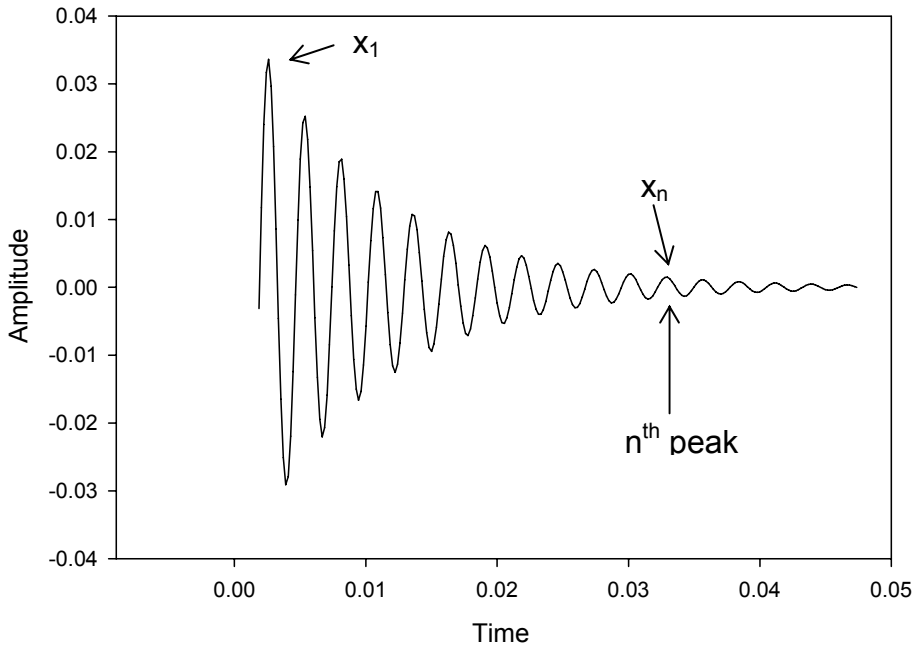


*Figure 2. Logarithmic decrement (free vibration).*

Q is subsequently calculated using the damping ratio ζ or the constants of the differential equation, using

$$Q = \frac{\sqrt{km}}{b} = \frac{1}{2\varsigma} \tag{6}$$

$$\varsigma = \frac{b}{2\sqrt{km}}. \tag{7}$$

The quality factor of a few MEMS systems that are designed to operate at resonance are found in literature. Q can be affected by numerous parameters of each device including operating environment (viscosity, temperature, pressure) and device dimensions, materials, processing and control electronics. The most common MEMS devices whose Q values are reported in literature are capacitive micromachined ultrasonic transducers, or cMUTs. These devices are used to transduce electronic signals into acoustic signals, or vice versa. They tend to be arrays of small membranes fabricated using silicon technology. Usually the frequency spectra of these devices are reported in literature and used to estimate the Q of the device, and Q values range from 1-115 [26-32]. These devices differ from the P3 micro heat engine in their designated application, and therefore the method of calculating Q can be the same, but the values of Q have very different consequences for device operation.

Another device that uses Q as a figure of merit is the piezoelectric micromachined ultrasonic transducer, or pMUT. With these devices, the electronic properties of the device can be used to approximate Q using an equivalent circuit model. From these circuits, or directly measured from the device, Q can be found by plotting the impedance or admittance vs. frequency, with values ranging from 67-1000 [33-37].

Q can also be measured for resonating membranes, diaphragms or cantilevers, showing the influences of the medium around the membrane, the clamping conditions of the membrane, the residual stress of the membrane, and thickness of the membrane [38-46]. Values of Q for these devices range from 60-10,000. Finally, Q has also been

reported for thickness-shear-mode resonators [47]. This device had a Q of approximately 5800.

### *1.4 OBJECTIVES*

The objectives of this research are to investigate energy losses in the P3 micro heat engine, focusing specifically on the figure of merit quality factor, Q, which depends directly on the mass, damping and stiffness of the system. These energy losses illuminate how the engine is operating, and which parameters influence energy loss during operation. Engine parameters are studied including cavity thickness, initial deflection, upper membrane size, bubble size, and heat input. Each of these parameters contributes to energy losses in the engine during operation. To discover the trends of engine energy loss, these parameters are varied, and the effect on Q is observed. A parametric study is undertaken to determine how Q varies with each engine parameter. Energy losses in the engine are characterized and quantified using Q, but come from many different sources including friction losses, heat transfer losses, and viscous dissipation. All of these losses are included in the value of Q. By analyzing the trends of Q with different engine parameters, and extrapolating with a linearly coupled oscillator model, optimization can yield the best configuration for a particular application to minimize energy loss.

# CHAPTER TWO
# FABRICATION AND ENGINE BASICS

The P3 engine design is based on flexing membranes, as previously mentioned. The microfabrication process is where the whole engine assembly and testing sequence begins. Engine basic operating characteristics depend on the accuracy and consistency of the microfabrication process. See Appendix for complete detailed fabrication steps. After the microfabrication is detailed, the engine testing and experimental setup, including resonance and Q testing, can be completed.

## *2.1 ENGINE FABRICATION*

The heater membranes and bare Si membranes are fabricated from 3 inch Silicon wafers. Silicon is used because the microfabrication processes are well-developed from the microelectronics industry, and high tolerances can be obtained. All of the processing for these membranes is done at WSU in the cleanroom. A diagram of the fabrication process is shown in Figure 3.

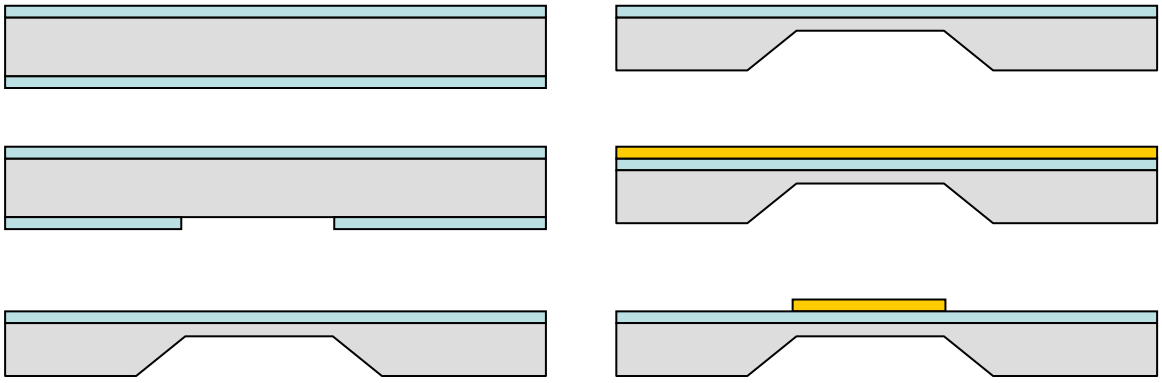


*Figure 3. Fabrication process diagrams. (a) Bare Si membranes (b) Heater membranes.*

First, the wafer is doped with boron in a furnace to a depth of approximately 2µm. Then the wafer is oxidized in a low temperature wet oxidation process, so that the resulting silicon oxide layer is approximately 150nm. Next, the oxide is patterned using

standard contact photolithography and BOE etching. Once the oxide is patterned, the membranes are formed using a silicon etch, either EDP or KOH. Etching removes all of the silicon from the back side of the wafer up to the boron etch stop, leaving a 2μm thick membrane. This completes the bare Si membranes.

To make a heater wafer, the bare Si membrane is sputtered with a 5nm TiW adhesion layer and then 300nm of Au. The Au is then patterned into a resistance heater pattern using the same photolithography processing as the oxide patterning and a gold etchant. The adhesion layer is also removed, and the wafer is finally cleaned. After dicing the wafer into dies, the heaters are ready to use. A typical resistance value of a heater is around 70-300Ω, depending on the pattern. Figure 4 shows example mask patterns used to make bare Si membranes and heaters, and Figure 5 shows an actual heater die.

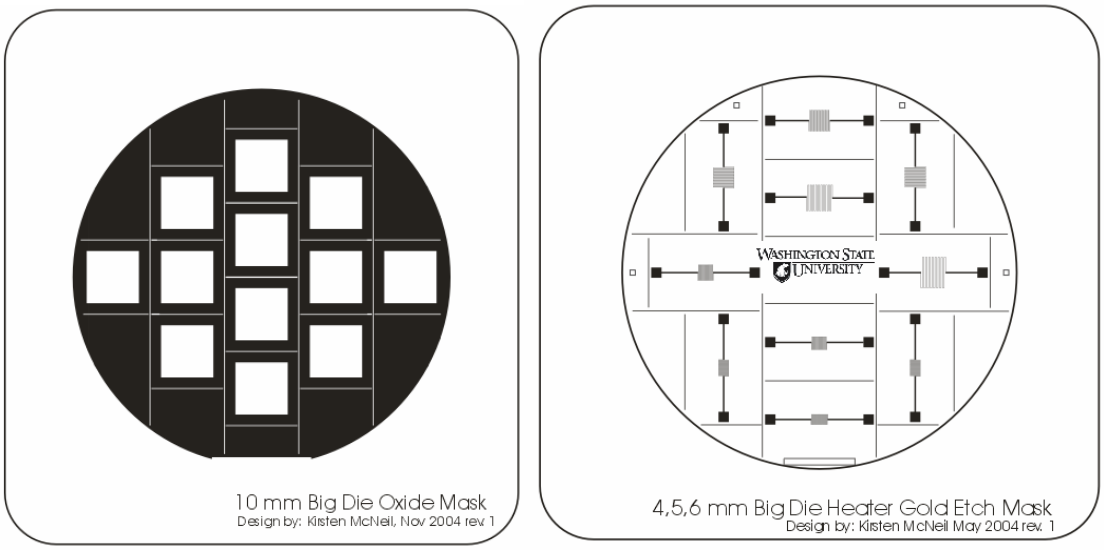


*(a)* *(b)*

*Figure 4. Example mask patterns for (a) 10mm bare Si membranes and (b) 4, 5, and 6mm heater membranes.*

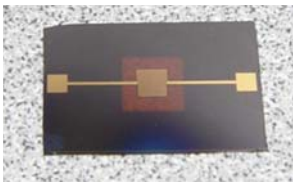

*Figure 5. Typical heater die, 6mm membrane. Electrical resistance ~ 200Ω.*

### *2.2 ENGINE BASICS*

The micro heat engine consists of two flexible membranes separated by a cavity defined by semiconductor tape. The experimental configuration uses a bare silicon membrane as the top membrane and a lower silicon membrane with patterned gold for use as a resistance heater. A bare naked silicon membrane is used to allow the experimenter to view the bubble inside the engine, as the membrane is transparent.

An engine is defined by the parameters of upper/lower membrane size, cavity thickness, bubble size and initial deflection. If the same membranes are used in several different engine assemblies, the engines may not have the same characteristics. Each assembly is defined as a new engine because the amount of fluid in the engine is not known exactly. The bubble is formed by allowing some of the liquid to evaporate and become vapor prior to sealing. The liquid used in the engine cavity, PF-5060 by 3M, has a very low boiling temperature (56ºC) and readily evaporates at room temperature and pressure. We use this to our advantage to make optimal size bubbles inside the engine. The working principle behind the engine is that when heat is input, the heat goes into evaporating the liquid and changes it into a vapor. This phase change makes the upper membrane expand. The size of the bubble therefore affects where the heat should be input to get the maximum amount of phase change, because this phase change produces the greatest amount of expansion.

Typically, engine membranes are different sizes. The upper membrane is larger, and therefore more compliant [48], so that most of the useful work done during operation is achieved by the upper membrane. The lower membrane size is chosen so that the stiffness is a sufficient amount greater than the upper membrane to make this assumption valid. In the experiments reported here, 10mm upper and 6mm lower membranes were used. Figure 6 shows a diagram of engine components.

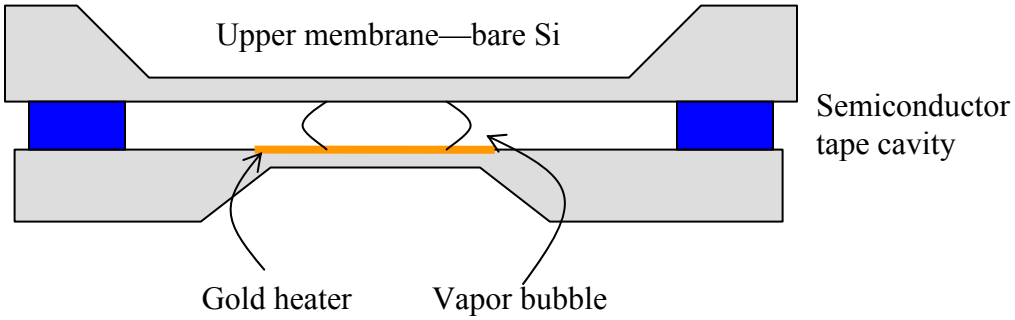


*Figure 6. Engine component diagram.*

The testing parameters that are defined during a set of engine tests include the applied voltage, duty cycle, frequency, physical engine parameters described above, and the settings on the laser vibrometer which determine the scaling of the output voltage. All of these are defined by the experimenter. The output of the experiment is a voltage-time signal of the deflection, velocity and input of the engine. These are captured with the oscilloscope and transferred into CSV files. The laser vibrometer has a resolution on the scale of picometers, and the oscilloscope outputs 2500 data points for each screen capture.

The laser vibrometer measures the deflection and velocity of the upper membrane during an engine test. It is assumed that the lower, smaller membrane deflects slightly less during the test, and is neglected. The lower membrane is free to deflect, however.

For a given pressure in the engine, the lower membrane will deflect less than the upper membrane, based on their stiffnesses. The engine parameters like initial deflection and volume of the cavity are also assumed to not change during testing. Complete experimental details are discussed in Chapter 3.

### *2.2.1 Assembly*

An engine consists of four major parts: membranes, cavity, fluid, and assembly jig. Figure 6 shows a schematic of the engine components. The upper and lower membranes are made by the process detailed in the section 2.1. The cavity of an engine is cut out of semiconductor tape, and centered around and secured to the bottom membrane. The width of the cavity tape should be 2-3mm. If more than one layer is required, a second cavity is cut and placed on top of the other one. For engine assembly, the heater is taped to the bottom half of an acrylic engine carrier. This carrier, shown in Figure 7, allows the experimenter to handle the engines during testing, functions as a place to attach engine probes to apply voltage to the heater, and clamps the membranes together to seal in the liquid.

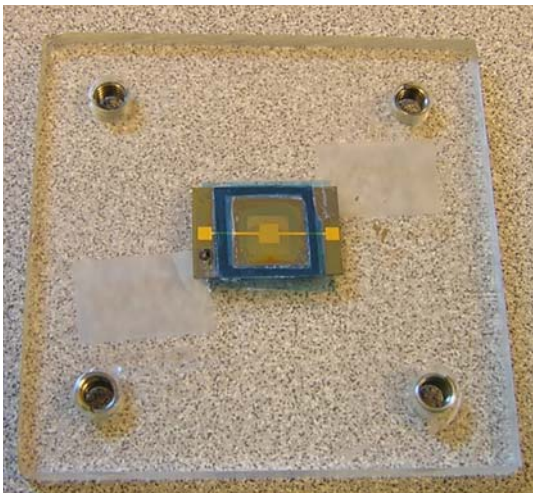

*Figure 7. Engine carrier with heater.*

After the heater is taped onto the bottom carrier, PF-5060 is squirted into the engine cavity and the upper membrane is quickly slid into place, pit side up. The membrane is situated in this way so that the flat side of the die can seal well with the cavity. To complete assembly, an o-ring is placed around the pit of the upper membrane and then the upper carrier is then screwed carefully together with the lower carrier.

The o-ring used in engine testing should be slightly smaller in diameter than the diagonal length of the upper membrane. This way the o-ring sits directly above the semiconductor tape of the cavity. This has been found to provide the best seal. If this does not seal the engine well enough, a slightly larger o-ring can be used.

The engine carrier should be tightened just enough to provide a good seal for the engine. Tightening the carrier too much can crack the engine membranes. Tightening too little can cause the engine to leak. A proper tightness is obtained when the experimenter can see uniform contact between the o-ring and upper carrier.

Different techniques exist for obtaining the proper size bubble inside the engine during assembly. The key step is the exact timing of when the upper membrane is placed over the cavity. If the liquid in the engine is allowed to evaporate for a few seconds before the upper membrane is place on, this usually yields larger bubbles. The time at which the upper membrane is placed on the cavity and the geometry when the membrane is placed there are the key factors in determining the bubble size.

The initial deflection can also be adjusted by the assembly technique. The initial deflection of the engine is determined by the volume of fluid in the engine and the pressure at which the two engine carriers are screwed together. It can be manipulated by

changing the time at which the two membranes are brought together, and the time when the top carrier is screwed down completely.

### *2.2.2 Sealing*

Absolutely necessary for successful testing is getting the engines to seal well. Sealing has been a major problem with larger engine sizes. To overcome this, a tacky substance (silicone-based heat sink compound) was regularly applied to the semiconductor cavity to get better contact between it and the upper membrane die. This was found to not affect the outcome of the experiments, while yielding a very good engine seal. This method was frequently used as needed for the data reported here. If the engine does not seal well during testing, the ringout results can change over the course of a few minutes, causing inconsistent and unusable data.

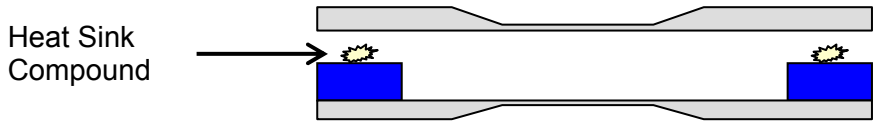


*Figure 8. Location of heat sink compound for sealing.*

# CHAPTER THREE
# EXPERIMENTAL TESTING

Once microfabrication has produced viable membranes and heaters, engine testing can be undertaken. Experimental testing serves several different purposes: measuring the resonant frequency of the engine, calculating Q of the engine, and/or running the engine at a specified frequency to measure its dynamic characteristics. This work focuses on the energy losses during one ringout, quantified by the Q and percent friction of the engine. Some analysis of the data after experimentation is required to produce these quantities.

## *3.1 ENGINE TESTING*

Engine testing begins after a good engine is assembled and sealing well. The heater die is designed so that the contact pads on either side are unobstructed when the upper membrane is sealed to the cavity. To begin testing, the engine probes are brought into contact with the contact pads on the heater, attached to the engine carrier via magnets, and the assembly is hooked up to the equipment. Figure 9 shows the engine assembled and in the engine carrier, ready for testing. Care should be taken when bringing the probes into contact with the heater pads, as sometimes the gold can be scratched easily, which can ruin the heater by creating a break between the pad and the heater lines.

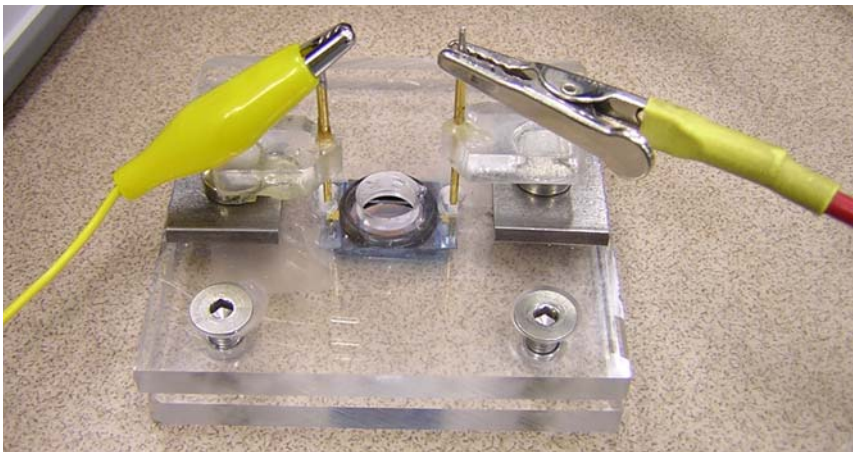

*Figure 9. Engine assembled in carrier ready for testing.*

The equipment, shown in Figure 10, should be tested prior to attaching the probes to make sure voltage will not flow uninhibited into the heater. Because of the setup between the TTL circuit and the AFG (arbitrary function generator), 9V can flow from the TTL circuit plug straight into the heater if the equipment is not set up correctly, destroying the engine within seconds. This can be checked by applying ~5V from the power supply and touching the two probes that will go to the heater together while watching the current on the power supply. The current should be zero if the circuitry is hooked up correctly. The correct wiring is shown in Figure 10. It is the initial setting on the AFG output that will make the engine overheat. The output must be turned on in order to keep the 9V from flowing into the engine uninhibited.

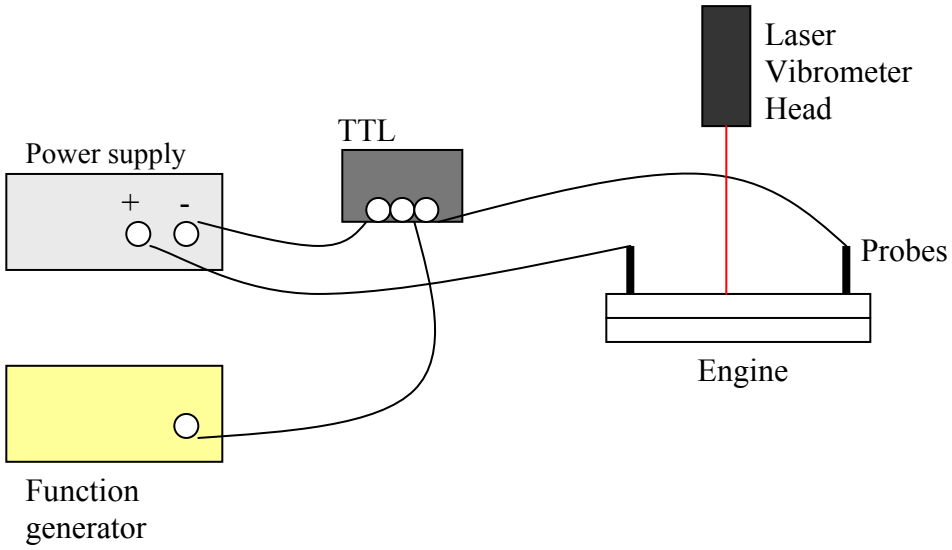


*Figure 10. Engine testing equipment setup.*

The TTL circuit [49] in the engine test setup is designed for ease of single shot testing. The TTL circuit is placed between the power supply and the engine, so that the voltage going to the engine can be precisely controlled by the AFG trigger. This way the power supply can be set to 30V, but the engine only sees that voltage when the TTL circuit is tripped by the experimenter, using the AFG trigger. Example experimental equipment settings are summarized in Table 1.

*Table 1. Experimental equipment settings.*

| Equipment | Example Settings |
|---|---|
| Power Supply | 30V |
| Function Generator | 100Hz, 2%, 4.5V, TRIG OFF |
| Laser Vibrometer | 16μm/V, 50mm/s/V, fast tracking filter |

These settings are chosen through experimental optimization and equipment and material limitations. The voltage applied to the heater is limited by both equipment and material properties. The power supply used in experiments could only apply up to 35V, and any voltage higher than this was found to often cause the heater to short and fail. The

pulse characteristics of the voltage into the heater were designed to apply a 200μsec pulse at an amplitude of 4.5V, the voltage required to trip the TTL circuit. This duration of pulse was chosen to sufficiently approximate an impact on the upper membrane. The laser vibrometer settings for velocity and deflection measurement are chosen to provide appropriate sensitivity to yield accurate results.

### *3.1.1 Initial deflection measurement technique*

The initial deflection of the engine is measured by moving the laser spot from the edge of the membrane to the center, and measuring the change in deflection voltage real-time on the oscilloscope. This method yielded fairly consistent results. A new, more precise method was developed which greatly improved the repeatability of this measurement. As shown in Figure 11, the new method moves the laser spot from the center of the membrane exactly 4mm towards the edge, so it doesn't measure the absolute initial deflection, but within the uncertainty of ± 3μm. The tracking filter on the laser vibrometer must be set to "fast" for this measurement to yield consistent results. This tracking filter reduces brief dropouts and noise in the real-time signal during initial deflection measurement [50].

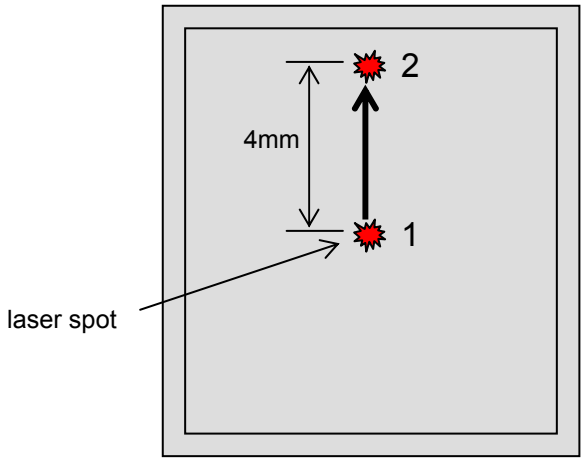


*Figure 11. Initial deflection measurement technique diagram for 10mm upper membrane using laser vibrometer.*

### *3.1.2 Bubble size measurement technique*

The size of the bubble in the engine is measured by visual inspection. Gold lines patterned for the heater membrane serve as a good reference when judging the size of the bubble. Most heater lines form a shape smaller than the total size of the heater membrane, yielding a good reference as well. Figure 12 is a picture of a bubble inside an engine. Bubble sizes were measured using a ruler and referencing the gold lines on the heater membrane, yielding an uncertainty of ± 300μm, as measured in this work. A more precise measurement could be achieved by using imaging software.

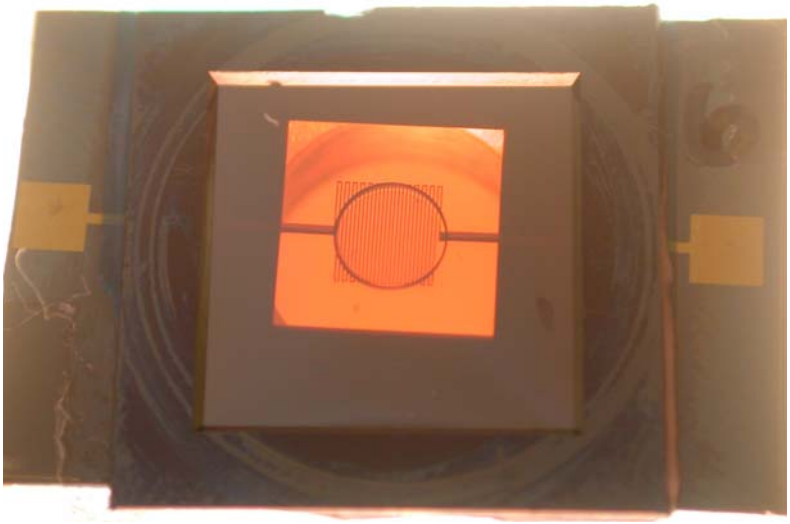

*Figure 12. Bubble inside engine (3mm bubble).*

## *3.2 LASER VIBROMETER*

The laser vibrometer used in these experiments operates on the principle of Doppler shift of the laser light being reflected off of the sample. In this case, the sample is the upper membrane of the engine. Internally, the generated helium-neon laser beam is split into a reference beam and an experimental beam. A diagram is shown in Figure 13. The experimental beam is the laser light that is reflected off of the sample, which is detected in the sensor head, and then the two beams are compared. Two beams of

coherent light combining will cause interference of a specified frequency. When the two beams combine, an interference pattern is measured. This interference pattern is transduced into an electrical signal through a photo detector. The vibrometer computer then uses this interference frequency to calculate the deflection and velocity of the phase change in the experimental beam, which are displayed for the experimenter. For some tests, an electronic filter was used to remove 60Hz and high frequency noise in the displacement signal.

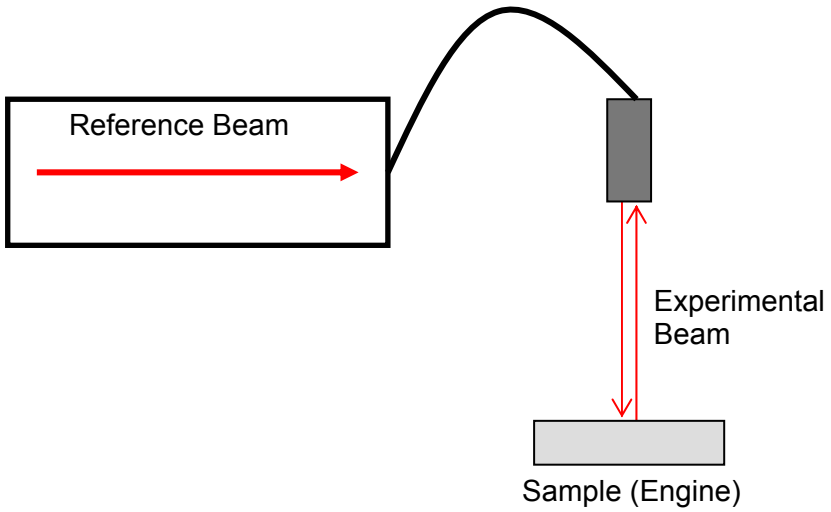


*Figure 13. Operating principle of laser vibrometer for velocity measurement.*

### *3.3 RINGOUT TESTING*

To measure an engine's resonant frequency, a ringout is performed. This free vibration response of the engine will yield the resonant frequency as well as Q and % friction of the specific engine assembled. A ringout imposes an impact on the upper membrane by evaporating liquid and causing the engine cavity to expand very quickly. This expansion is followed by rapid contraction, and the upper membrane consequently vibrates at its natural frequency. The testing equipment should therefore be set to input a very short heat pulse to the resistance heater (200µsec), at the tester's will. A forced

trigger setting on the AFG will make this possible. The heat pulse duration and amplitude are defined by the settings on the AFG and power supply. For example, to send a 30V 200µsec heat pulse into the engine, the AFG should be set to 100Hz and 2% duty cycle, as detailed in Table 1. The power supply controls the amplitude, so this should be set to 30V in this case. See Figure 14 for an example heat pulse. The deflection and velocity of the resulting ringout are of interest, so both should be measured from the vibrometer. Often the velocity would yield better ringout results because it is centered about zero.

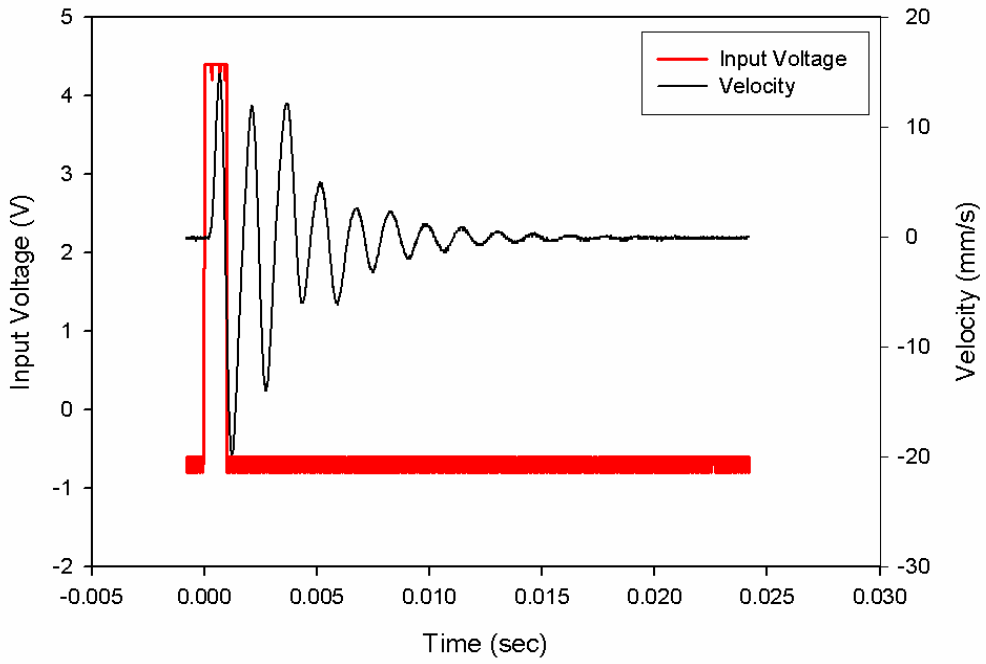


*Figure 14. Example ringout data. 10mm engine, 37V input.*

Internal vibrometer settings were chosen to ensure sufficient accuracy of experimental data. The deflection was set to a resolution of 16µm/V and the velocity was set to 50mm/s/V and the voltage output of the vibrometer was multiplied by these conversions to get deflection and velocity. Typical deflections and velocities measured during ringout testing were 1µm and 25mm/s, so these settings allowed for sufficient accuracy in the measurement, without too great of a resolution.

The key to engine testing is consistent assembly. Usually a set of data was desired that held all but one engine parameter constant. For example, if a data set was needed that examined the effect of bubble size on resonant frequency or Q, only engines with all other parameters held constant would be tested. It is a trial-and-error method used to assemble engines with a specific bubble size or initial deflection. These parameters can be controlled with patience and practice, again in a trial-and-error fashion. Once an engine is assembled, the probes are attached and the laser is centered on the upper membrane. If the initial deflection is to be measured, it is done so before the heat is pulsed into the engine.

### *3.3.1 Ringout measurement technique*

A heat pulse is designed as previously described, and the oscilloscope trigger is set to measure this pulse and trigger when it is applied by the tester. The oscilloscope settings can scale the velocity and deflection output from the laser vibrometer, so care must be taken. The program WaveStar for Oscilloscopes (Tektronix) was used to capture data from the oscilloscope to the computer through a GPIB-USB port, and exported as a CSV file. This method gives 2500 data points for the YT (y-amplitude, time) plot, which usually spans about 0.02sec.

## *3.4 ENGINE RUNNING*

For dynamic engine operation, different experimental settings need to be used. In this situation, the engine receives a constant input of short heat pulses, with a duty cycle and frequency set to any value of interest, and the dynamic deflection and velocity signals can be measured. An example set of data is shown in Figure 15 for comparison to ringout data.

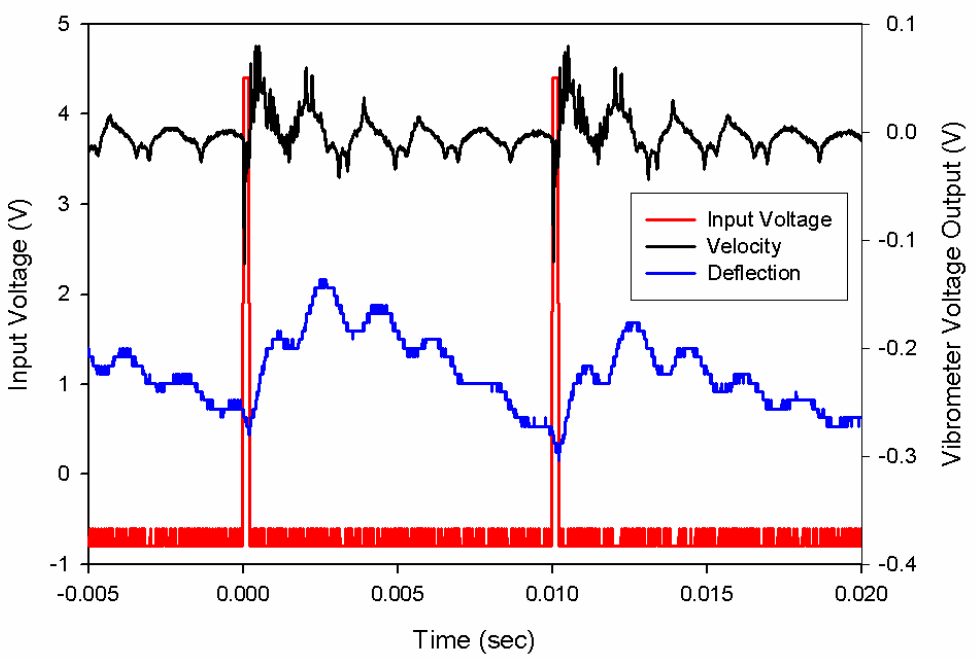


*Figure 15. 10mm engine running, 100Hz, 16V input.*
*(velocity: 50mm/s/V, deflection: 16µm/V)*

Figure 15 shows that engine running is very different than ringout testing. The velocity shows a clear vibration signal, with some noise in the data, but the deflection signal shows an overall shape as well as the natural frequency vibrations. During running, the constant input of heat pulses does not give the engine the same amount of time for the vibrations to damp out like during ringout testing. This effect increases in magnitude as the running frequency is increased. Ringout and Q testing is designed to describe what will happen between the heat pulses during engine running, which is how the engine will operate in application.

### *3.5 DATA PROCESSING*

After the YT data is exported to the computer, data analysis must be performed to determine the final results of the testing. The laser vibrometer has a scale setting which converts its voltage output to absolute µm for deflection and mm/s for velocity. These

values must be recorded from the vibrometer, as they are not output with the data. Scaling the vibrometer voltage output and plotting yields results similar to those seen in the example ringout in Figure 14. Curve fitting the ringout data with a damped sine wave in SigmaPlot is used to calculate Q. The damped sine wave has the form

$$y = ae^{\left(\frac{-x}{d}\right)} \sin\left(\frac{2\pi x}{b_c} + c\right) \tag{8}$$

where a, $b_c$, c, and d are constants calculated in the curve fit, and this $b_c$ should not be confused with the damping parameter b. Resonance can be calculated from the damped sine wave curve fit parameters using

$$f_r = \frac{1}{b_c} \tag{9}$$

which is equal to

$$f_r = \frac{1}{2\pi}\sqrt{\frac{k}{m}} \tag{10}$$

and Q is calculated using the constants $b_c$ and d in the relation

$$Q = \frac{\pi d}{b_c} = \frac{\sqrt{km}}{b}. \tag{11}$$

The curve fit parameters correspond to the differential equation parameters as detailed in Table 2.

*Table 2. Correlation between differential equation and curve fit parameters.*

| Curve Fit Parameter | Differential Equation Parameter |
|---|---|
| $b_c$ | $\frac{1}{f} = 2\pi\sqrt{\frac{m}{k}}$ |
| d | $\frac{1}{2\pi f\zeta} = \frac{2m}{b}$ |

SigmaPlot uses an iterative Marquardt-Levenberg algorithm (least-squares method), beginning from a guessed value, to find the best fit between the equation and the data. Once convergence is achieved, the curve fit parameters are defined [51]. Quality of fit can be estimated by the R squared value reported when the curve is fit to the data. Common R squared values of curve fits reported here range from 0.4-0.7, indicating a fairly poor fit, but as can be seen in Figure 16, the curve fit follows the important experimental data parameters closely, amplitude and frequency. The most important parameters of the curve to fit are the amplitude and the frequency. As long as these values match fairly well, good curve fit results can be obtained.

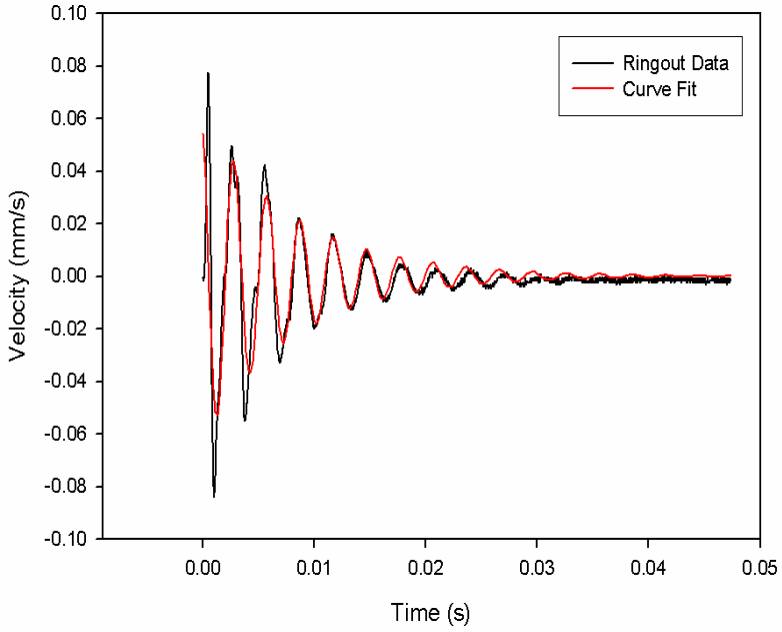


*Figure 16. Example curve fit of ringout data.*

# CHAPTER FOUR
# CALCULATIONAL METHODS

Experimental data are analyzed to complete the description of how the engine is operating during testing. Data from one ringout can be analyzed in several different ways to reach different goals. For example, one ringout can be used to calculate resonance, Q, percent friction and several other parameters of interest during engine operation. After the data have been analyzed, statistical methods are used to develop trends in the data and compare different engine configurations.

## *4.1 DATA ANALYSIS*

### *4.1.1 Resonance and Q calculations*

The resonant frequency of an engine is the first mode of vibration, the frequency at which the most output (deflection in this case) is seen for a given input (voltage into heater). When a heat pulse is applied to the heater in the engine, the resulting impact on the upper membrane causes it to vibrate at its resonant frequency. Because the pulse is very short, and does not continue to force the system, the vibration damps out over time. The resonant frequency can be measured from this ringout, using $f = 1/\Delta t$.

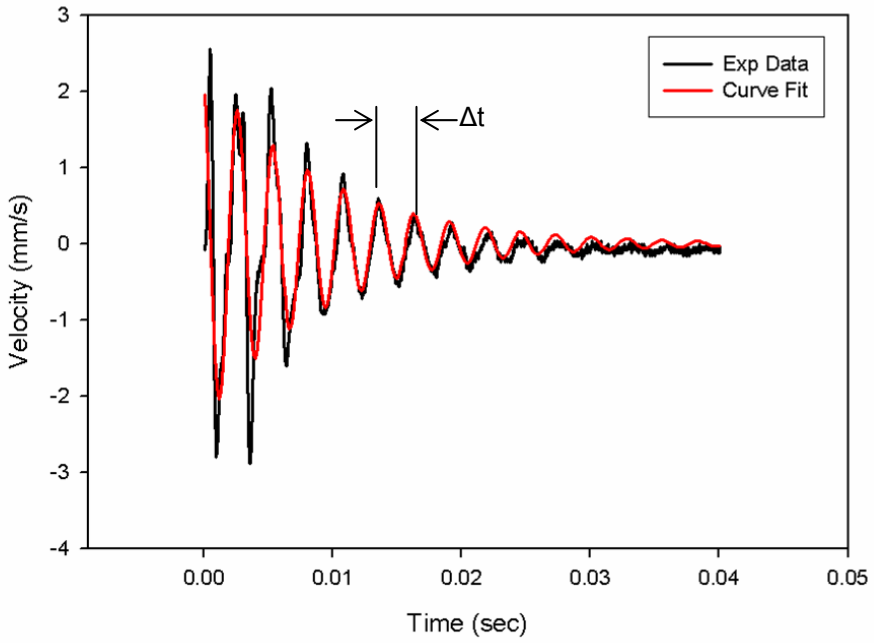


*Figure 17. Sample ringout and curve fit in SigmaPlot.*

The above figure shows a sample ringout and damped sine curve fit in SigmaPlot. The curve fit yields parameters, see section 3.5, which can be used to calculate the characteristics of the ringout including resonant frequency, effective mass, damping coefficient, Q and % friction.

For example, a typical ringout curve fit is given by

$$y = (1.1585e-8)e^{\left(\frac{-x}{0.011083}\right)} \sin\left[\frac{2\pi x}{0.002736} - 0.1349\right]. \qquad (12)$$

Comparing this with Equation (8) shows that the constants $b_c$ and d are 0.002736 and 0.011083 respectively. These curve fit values yield a resonant frequency of 365Hz and Q of 12.7, using the equations in section 3.5.

### *4.2 COMPARISON OF Q CALCULATION METHODS*

The quality factor of a resonating device can be physically measured using several different methods. A piezoelectric cantilever, shown in Figure 18, with dimensions 50mm

x 25mm x 1mm, was used to compare these measurement techniques to determine their consistency and accuracy. Not all of these methods are available to measure the Q of the P3 engine, however.

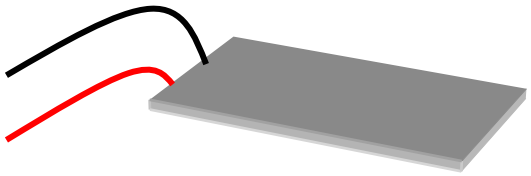

*Figure 18. Piezoelectric cantilever used in Q calculation comparison.*

Five techniques were used to measure the Q of the cantilever/bender: mechanical impulse, electrical impulse, manual frequency sweep, sine signal sweep/chirp, and using the electrical characteristic parameters. The first two methods apply an impulse to the bender, either mechanically or electrically. The resulting deflection ringout is measured with the laser vibrometer. A curve fit is then applied using the method detailed in the previous section to calculate Q. The manual frequency sweep is determined by the operator. The test frequency range was chosen to be +/- 20Hz of the resonant frequency. At each frequency over a determined range a voltage is manually applied to the bender and the resulting deflection (amplitude) is measured. The operator increments the input frequency, applies the same voltage, and measures the deflection again. Q is then calculated using the spectrum, similar to Figure 1. The three frequencies $f_1$, $f_2$ and $f_r$ defined in Figure 1 are calculated using the amplitude and Q is found using

$$Q = \frac{f_r}{f_2 - f_1}. \qquad (13)$$

The sine signal sweep method uses the function generator to apply frequencies between 1-1000Hz, chosen because the resonant frequency of the bender used was around 75Hz, the deflection is measured, and Q is calculated similarly to the manual frequency sweep.

The final method calculates the electrical quality factor, $Q_e$ using the electrical characteristics of the bender [52]

$$Q_e = \frac{1}{R_m}\sqrt{\frac{L_m}{C_m}} \tag{14}$$

where R, L, and C are the electrical equivalent circuit parameters. These values can be found from analyzing the impedance curve of the bender, detailed in [45]. Each of these methods yielded slightly different values of Q under the same conditions for the bender. The measured Q values using each technique are shown in Table 3. The results show each technique will report the same Q value, ±15%.

*Table 3. Comparison of Q measurement methods.*

| | Mechanical Impulse | Electrical Impulse | Manual Frequency Sweep | Sine Signal Sweep | Electrical Q |
|---|---|---|---|---|---|
| Q | 37.7 | 44.5 | 36.0 | 37.5 | 39 |

### *4.3 ANOVA*

A statistical analysis of variance (ANOVA) method was used to determine trends in the parametric study. Analysis of variance compares the means of several data sets to see if there is a statistical difference between them. This method requires that each data set have the same number of data points. A hypothesis is proposed that the means of each data set are the same. This would mean there is no difference in the data for each treatment. After the data has been assembled, the means of each set are calculated. Then several parameters comparing the means of each set with individual values are calculated. These parameters are the variation between treatments, the variation within treatments, and the total variation. The grand mean, or the average of the average of each data set, is also calculated. From these parameters, the degrees of freedom are calculated according to the formulas, the mean square of the first two variations is found, and the Fisher

variable is found using the Fisher distribution table. The Fisher variable is compared with the corresponding variables at the 95 and 99 percent confidence levels, and the original hypothesis is tested. If the calculated Fisher variable is lower than the 95% confidence level, the hypothesis is rejected. If the variable lies between the confidence levels, the hypothesis is accepted at the 95% level. If the variable is higher than the 99% level, the hypothesis is accepted at that level. An example calculation is given in section 4.3.1.

### *4.3.1 Example ANOVA calculation*

Q data was used in the statistical analysis to form definitive trends. The following is an example ANOVA calculation using Q data from Figure 27.

*Table 4. Q data for ANOVA analysis.*

| **Treatment: (Bubble Size)** | **Measured Values: (Q)** | | | | **Treatment Mean:** |
|---|---|---|---|---|---|
| 1mm | 12.73 | 17.09 | 16.72 | 12.21 | 14.69 |
| 2mm | 11.66 | 9.77 | 15.35 | 6.7 | 10.87 |
| 3mm | 10.4 | 11.32 | 11.84 | 11.68 | 11.31 |
| 4mm | 7.82 | 10.42 | 9.64 | 8.76 | 9.16 |

a = number of treatments = 4

b = number of sets = 4

Grand Mean: $\overline{X}$ (average of treatment means) = 11.5069

Total Variation: $V = \sum_{j,k} (x_{jk} - \overline{X})^2$ = 128.46

Variation Between Treatments: $V_B = b\sum_{j} (\overline{x_j} - \overline{X})^2$ = 64.27

Variation Within Treatments: $V_W = V - V_B$ = 64.19

*Table 5. ANOVA parameter calculation table.*

| **Variation** | **D.O.F.** | **Mean Square** | **F** |
|---|---|---|---|
| $V_B$ = 64.27 | a-1 = 3 | $V_B$ / (a-1) = 21.24 | =21.24/5.349 = 3.97 with 3 and 12 d.o.f. |
| $V_W$ = 64.19 | a(b-1) = 12 | $V_W$ / (ab-a) = 5.349 | |
| V = 128.46 | ab-1 = 15 | | |

From Fisher distribution tables:

$F_{.95} = 3.49$ (95% confidence)

$F_{.99} = 5.95$ (99% confidence)

The calculated F value above (right-hand side of Table 5) is between these two values, so the means of the data sets are "probably" different at the 95% confidence level.

## *4.4 PERCENT FRICTION*

### *4.4.1 Percent Friction Definition*

The quality factor is defined in terms of the energy stored and energy dissipated per cycle during a ringout,

$$Q = 2\pi \frac{energy\_stored}{energy\_dissipated}. \qquad (15)$$

The energy dissipated is the friction, so the ratio of the energy dissipated to the energy stored is the percentage of energy lost, or percent friction. Therefore the percent friction can be calculated using

$$\%f = \frac{2\pi}{Q} * 100. \qquad (16)$$

This approximation yields the percentage of energy lost during vibration of the engine. This "friction" in the engine is actually the energy lost from several sources, including viscous losses and internal damping in the membranes. This is another way of looking at losses in the engine, and can be directly calculated from the Q data presented in this work.

# CHAPTER FIVE
# DATA ANALYSIS AND RESULTS

Previous work is first summarized to put the current study in perspective. Results of a parametric study of engine parameters and their affect on energy loss are then presented and analyzed.

## *5.1 PREVIOUS DATA SUMMARY*

A parametric study on the engine resonant frequency has been previously completed. The resonant frequency of the engine is significant to this discussion because it is a key measure used to characterize each engine assembly. Resonance is affected by the geometry, materials and operating parameters of the engine. For this reason, a parametric study was completed by Robert Gifford [49] examining the effect of each of the following engine characteristics: membrane size, bubble size, and cavity thickness. The results conclusions are summarized here and in Table 6 for background.

Membrane Size: Four sizes of upper membrane were tested, with correspondingly smaller lower membrane sizes making up the engine. It was found that as membrane size increases, resonant frequency decreases. The 3mm engines were found to have an average resonant frequency of around 2700Hz, and 8mm engines, the few tested, were found to have a resonant frequency of 416Hz. This decrease in resonant frequency corresponds well with plate/membrane vibration theory [48]. This test was performed keeping all other engine variables constant.

Bubble Size: Engines with varying bubble sizes were assembled and tested, with bubble sizes ranging from 475μm to 1800μm. Every attempt was made to control the initial deflection during these experiments to make it constant. Although there is much

scatter in the data, the bubble size shows a slight trend with resonance. A change of 75% in the bubble diameter yields only an 8.2% change in resonant frequency. This is taking into account a 95% confidence interval around the data, and error bars corresponding to repeatability. This slight trend of resonance with bubble size may correspond to an increased mass of liquid when the bubble size is reduced, adding mass to the system and consequently decreasing the resonant frequency.

Cavity Thickness: The cavity thickness, or cavity depth, of the engine is controlled by the number of layers of semiconductor tape used to define the cavity. Each layer is 75μm thick, and engines with up to three layers were tested in this parametric study. Gifford notes [49] that it is increasingly difficult to assemble engines with thicker cavities, as the semiconductor tape is slightly compressible. This compressibility yielded higher initial deflections of the engines, altering the resonant frequency measurement. It was shown that engines with larger cavity thicknesses had higher resonant frequencies, and Gifford notes that this change in cavity thickness dominated over any change in initial deflection induced by the compressibility of the semiconductor tape.

*Table 6. Parametric study summary.*

| Parameter-trend: | Resonant Frequency trend |
|---|---|
| Membrane Size-increasing | Decreases |
| Bubble Size-increasing | Increases |
| Cavity Thickness-increasing | Increases |

### *5.2 WICK DATA: RINGOUTS AND Q*

Microchannel evaporators (wicks) are patterned on the bottom membrane (heater) in the engine using an epoxy. These channels create a more uniform and stable liquid layer over the heater and yield consistent evaporation results. The liquid layer over the

heater is very thin without the wicks and creating a thicker liquid layer yields more volume expansion for a given heat input, and therefore greater efficiency. A comparison was made to see if the presence of these wicks affects the resonance of the engine, because the epoxy does add stiffness and mass to the lower heater membrane. For these tests, 10µm high, 10µm wide "straight-shot" radial wick patterns were used. Figure 19 shows how the resonance changes with the addition of the wicks.

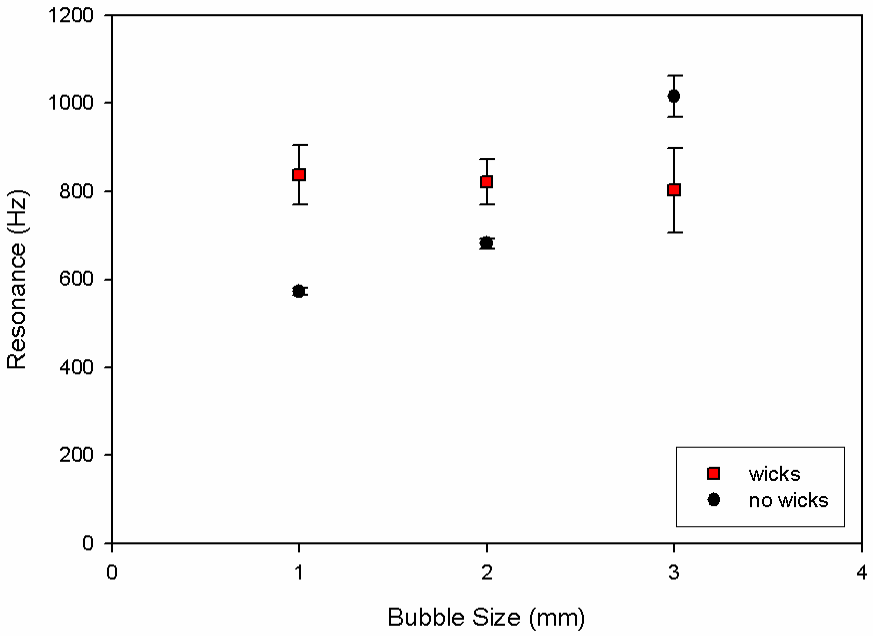


*Figure 19. Resonance of 6mm engines with and without wicks.*

The data in this figure consist of 6mm engines with radial wicks patterned on the heater membranes. The configuration of the engines tested was exactly the same except for the presence of the wicks. Several things can be seen in this figure. First, the wicks seem to make the resonance independent of bubble size. Second, the engines without wicks show a possible trend with bubble size, while the engines with wicks do not. The initial deflection was not controlled in these experiments.

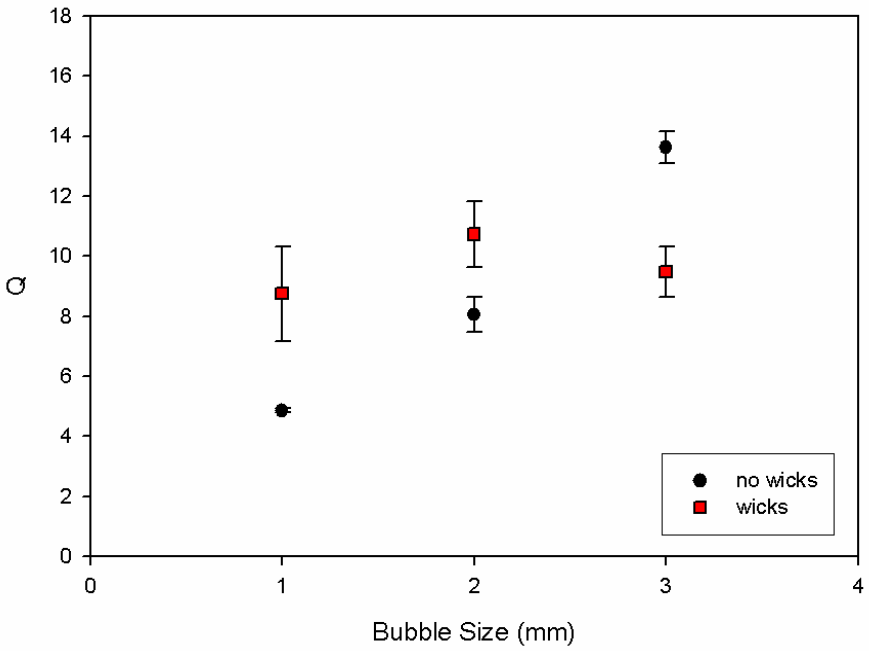


*Figure 20. Q of 6mm engines with and without wicks.*

The above figure shows the dependence of Q on bubble size and wicks for 6mm engines. Here Q is relatively independent of bubble size. However, these 6mm engine tests were not controlled as well, and the initial deflection was not measured. Therefore, only comparisons between these data are valid. No clear impact of the presence of wicks can be seen.

### *5.3 GENERATOR Q AND PERCENT FRICTION COMPARISON*

A membrane generator was also compared with a bare Si 6mm membrane. The generator is made of many different materials, has a very complex layered structure, and therefore very different stiffness than the bare Si membrane. This stiffness difference should affect Q.

*Table 7. Comparison of 6mm bare Si and membrane generator.*

| | 6mm Bare Si Membrane | 6mm Membrane Generator |
|---|---|---|
| Average Resonance (Hz) | 881 | 1423 |
| Average Quality Factor | 17.0 | 22.9 |
| Average Percent Friction | 36.9 | 27.5 |

As can be seen in Table 7, the increased stiffness of the membrane generator results in a higher resonant frequency, higher Q, and lower percent friction. This is yet another example of the interplay between stiffness and the quality factor. The interpretation of these results is that the generator with higher stiffness loses less energy during free vibration than the bare Si membrane. The generator has more mass and stiffness, which both would increase Q. Therefore, it can be assumed that the damping in both of these cases is about the same, and the stiffness and mass increases are what increase Q.

### *5.4 IMPACT RINGOUTS*

Another method was used to measure the resonant frequency of the engines. To verify that the heat addition and sudden evaporation are in fact acting as an impact on the upper membrane of the engine, a mechanical impact was applied instead, and the outputs were compared. This experimental testing setup is shown in Figure 21.

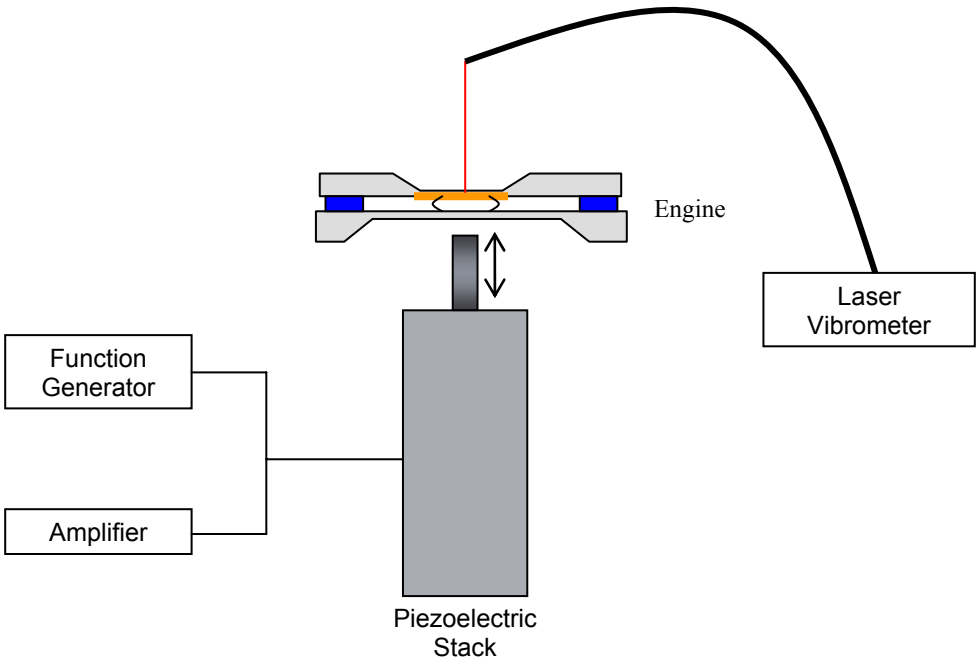


*Figure 21. Impact ringout experimental setup.*

A piezoelectric stack was used to impart an impact on the upper or lower membrane. The upper membrane was often used because of its larger surface area. The response of the heater/upper membrane was measured with the laser vibrometer as before. The response was characterized to determine how the piezoelectric stack affected the ringout of the engine, and whether the results were the same as for a heat ringout. A voltage pulse was sent to the stack to create the impact, and the distance away from the engine was closely calibrated. It was verified that the stack was moving away from the engine quickly enough as to not interfere with the ringout of the engine.

The resonant frequency of the piezoelectric stack was also measured, to verify that it was not interfering with the engine free vibration. This frequency, 1kHz, was far enough away from the engine's resonant frequency (~350Hz) so that they can be distinguished. As mentioned previously, the heater membrane and the upper membrane

were used for the impact. The measured resonant frequency of one engine when the heater was impacted was 300-330Hz, and when the upper 10mm membrane was impacted the resonant frequency was 330-390Hz. This verified that the resonant frequency of the engine is the same, regardless of which membrane is impacted. This shows that the resonance represents the entire system, not just the membrane that is measured. Many different 10mm engines were measured using the heat ringout method and the impact ringout method, and the resonant frequencies were found to be within ±50Hz, showing good agreement between the two methods.

### *5.5 Q AND PRESSURE*

Since Q depends on the stiffness and the damping present during an engine ringout, it should depend on the air pressure around the engine. This relationship has been extensively verified for many different vibrating structures [17,40,46,53,54]. An experiment was conducted where the engine was placed inside a vacuum chamber, and ringouts were measured as the pressure was decreased.

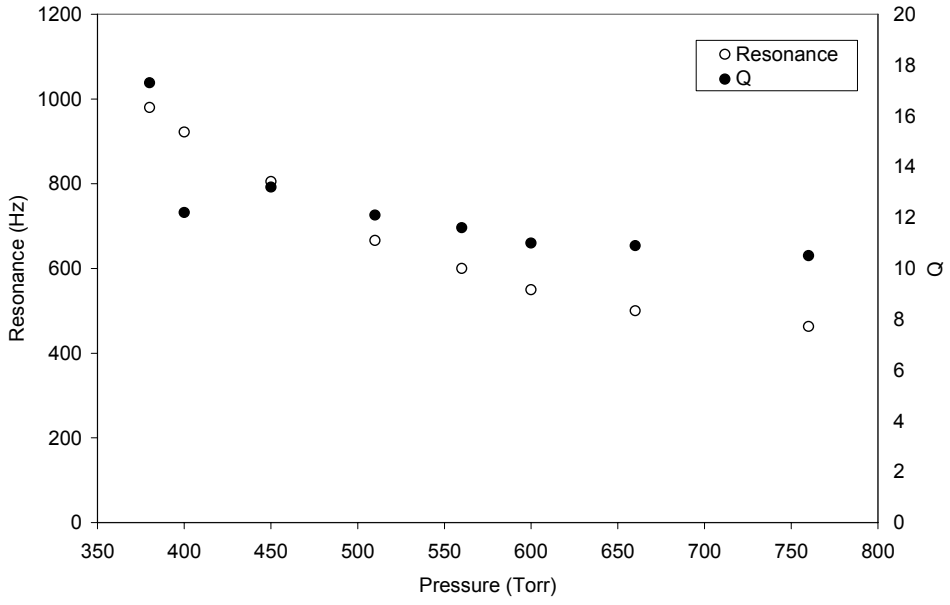


*Figure 22. Dependence of resonance and Q on pressure.*

As shown in Figure 22, the resonant frequency and Q both increase as the pressure decreases. This behavior is probably caused by the membranes bulging out due to the decrease in pressure around the engine, causing a higher effective stiffness. The viscous damping probably also decreases with pressure, as the air resistance on the free vibration of the engine is decreased. This would increase Q, as shown in Figure 22. The model in Chapter 6 will be used to de-couple these two effects. The variance of the data point at 400 Torr in Figure 22 is probably due to a pressure fluctuation or instrumentation fluctuation during measurement.

### *5.6 Q AND MEMBRANE SIZE*

The quality factor was computed for very many engine configurations. Engines of various sizes between 3mm to 10mm were tested and their Q values compared. Figure 23 shows that for multiple engine configurations, there is little correlation between Q and engine size. It should be kept in mind, however, that the only parameter held constant throughout this data was the cavity thickness, 150μm. A trend is expected with changing engine size, because the stiffness of the upper membrane changes, but so does the amount of liquid in the engine. The model in Chapter 6 is used to de-couple these factors.

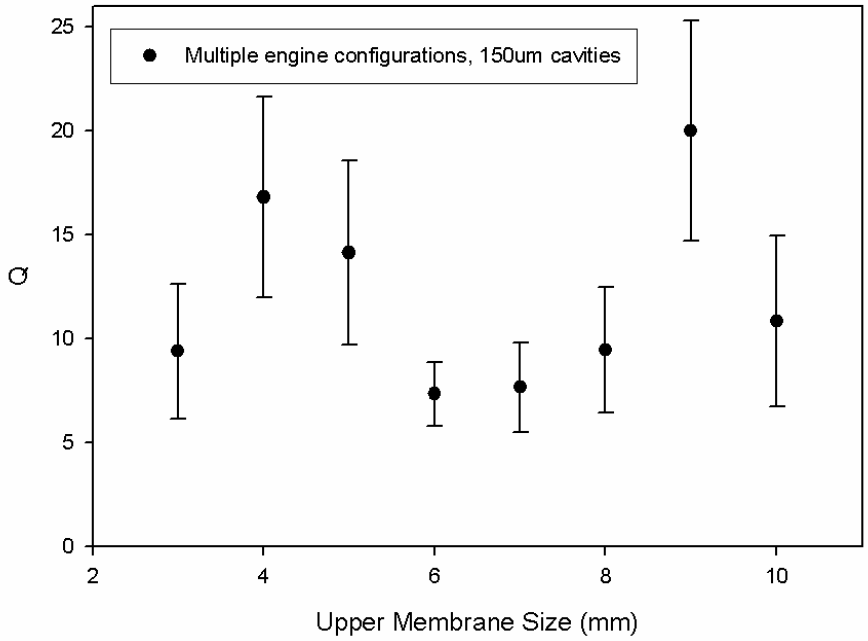


*Figure 23. Q and engine size for constant cavity thickness and multiple engine configurations.*

### *5.7 RESULTS: 10MM ENGINE Q PARAMETRIC STUDY*

The quality factor of an engine is determined from the ringout method. The quality factor is defined as the ratio of the energy lost to energy stored per cycle. This figure of merit defines the amount of energy losses during vibration of the engine. Therefore, measuring Q gives a slightly different measure of the energy losses of the engine structure. Engine parameters were isolated and tested to determine their effect on Q. This section covers a parametric study of engine parameters and their effect on Q.

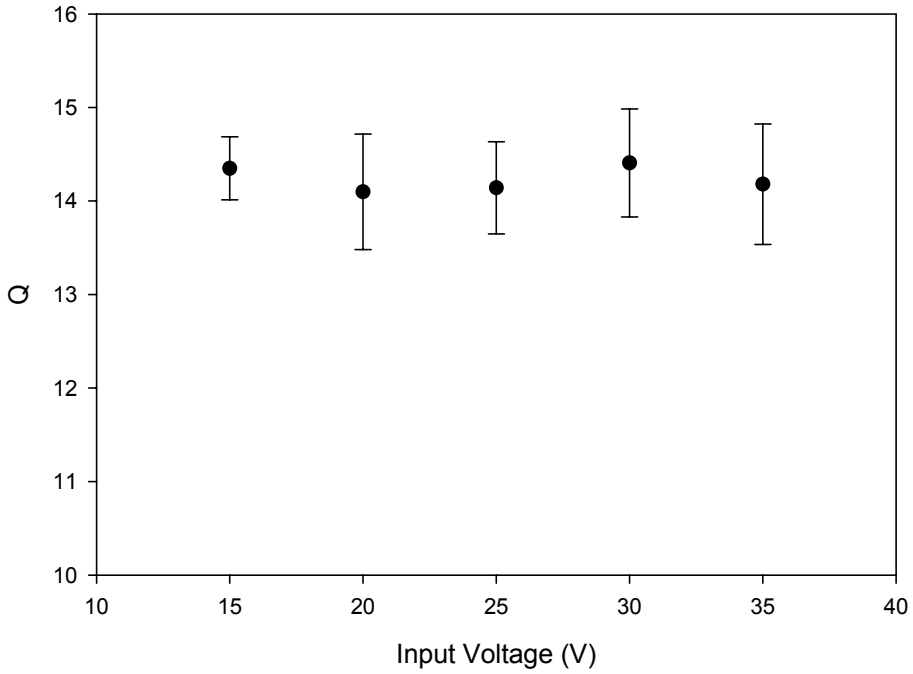


*Figure 24. Q dependence on electrical input voltage to heater.*

For this data set, all engine parameters were held constant except for the voltage applied to the heater. As can be seen in Figure 24, Q of the engine was relatively constant when different input voltages were applied to the heater. The error bars shown in the figure represent the standard deviation of each data set. Six engines were tested at each input voltage value. The input voltage to the heater determines how much energy is going into the engine during each ringout test, and input power can be estimated by using the input voltage and the resistance of the heater and Ohm's law.

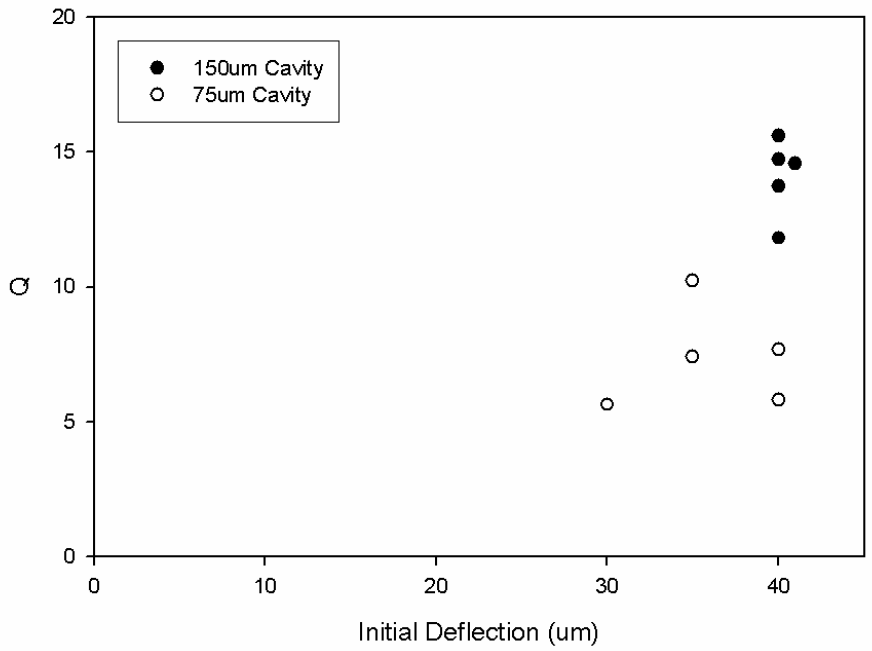


*Figure 25. Q dependence on engine cavity thickness for 75 and 150μm thick cavities.*

The above figure shows a clear trend of Q with cavity thickness. The cavity thickness of the engine is determined by the number of layers of semiconductor tape used to define the cavity, each layer being 75μm thick. Engines with a cavity thickness of 75μm have lower Q values than engines with a 150μm thick cavity, holding all other variables constant, including input voltage, bubble size and initial deflection. Using the differential equation parameters to define Q yields

$$Q = \frac{\sqrt{km}}{b}. \qquad (17)$$

An increase in Q could correspond to a decrease in damping (b) with a thicker cavity, or an increase in effective mass (m) or stiffness (k). The volume of liquid in the engine cavity increases for larger cavities, and this may add to the effective mass of the engine, while adding little damping, explaining the increase in Q. A linearly coupled oscillator model in Chapter 6 is used to determine which parameter is dominant.

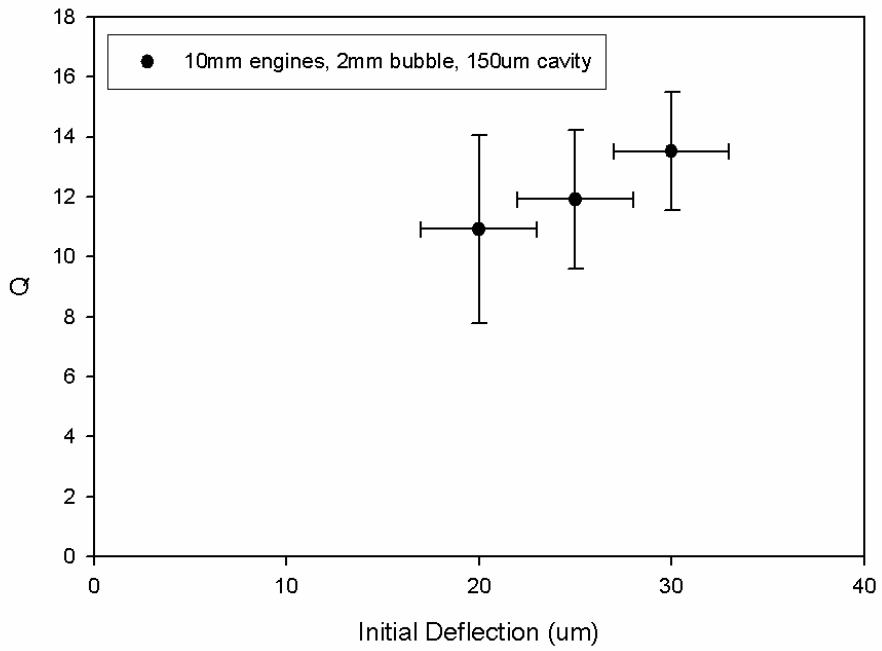


*Figure 26. Q dependence on engine initial deflection with 2mm bubble.*

Figure 26 shows the dependence of Q on engine initial deflection. Again, the initial deflection of the engine occurs during assembly because the pressure in the engine is greater than atmospheric pressure, causing the upper membrane to bulge slightly. For this data set, all other parameters were held constant, with bubble sizes of 2mm. The initial deflection of these engines was measured using the new technique described in section 3.1.1, resulting in much less scatter in the data than data taken earlier using the old technique. Still, each data set shows much variation with the error bars here being the standard deviation of each data set. Four to five engines were tested in each data set.

These results are consistent with Gifford's data [49] detailed in section 5.1 if we compare the initial deflection with membrane size. The key parameter in both cases is the membrane stiffness. It is evident from Equations (10) and (11) that resonance and Q both increase with increasing membrane stiffness. In Gifford's data, this corresponded to decreasing membrane size, and in Figure 26 stiffness correlates with initial deflection.

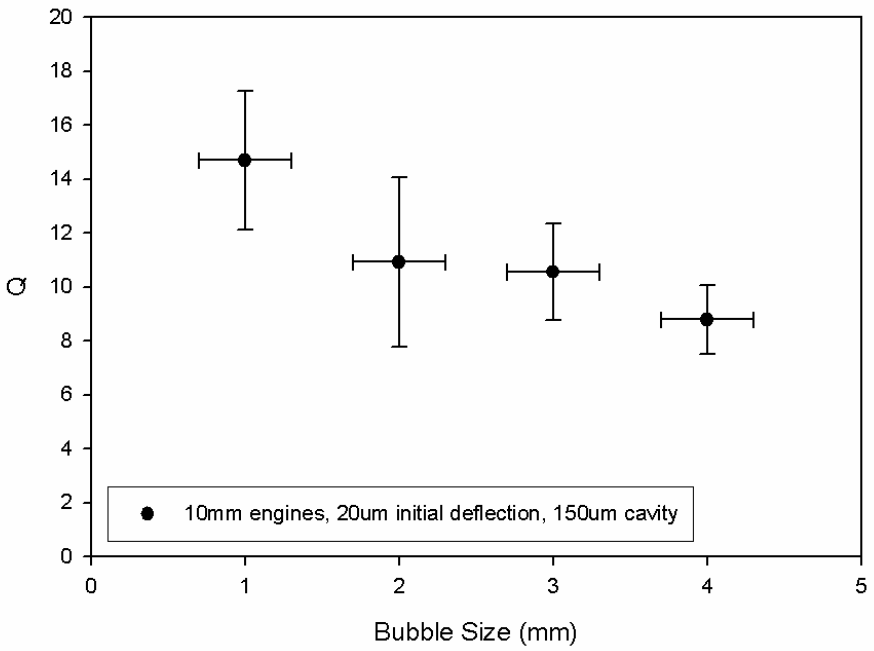


*Figure 27. Q dependence on engine bubble size with 20μm initial deflection.*

Here the dependence of Q on bubble size is investigated. The clear trend in Figure 27 shows Q decreasing with increasing bubble size. Four engines were tested at each bubble size value for this data set. When the bubble size increases, there is less liquid in the engine cavity. Liquid in the engine cavity increases the mass and possibly the stiffness of the system. Both of these changes would imply an increase in Q with decreasing bubble size. The size of the bubble may also increase damping in the engine, decreasing Q. The effect of each of these parameters was tested with the linearly coupled oscillator model, which will be discussed in Chapter 6.

The bubble in the engine was shown to slightly increase resonance with increasing bubble size. This could be due to an effect on either stiffness or mass, from Equation (10). From the trends seen, either increasing bubble size decreases the mass in the engine, increases the stiffness, or some combination of these. The linearly coupled

oscillator model in Chapter 6 will be able to de-couple these factors and determine which is dominant.

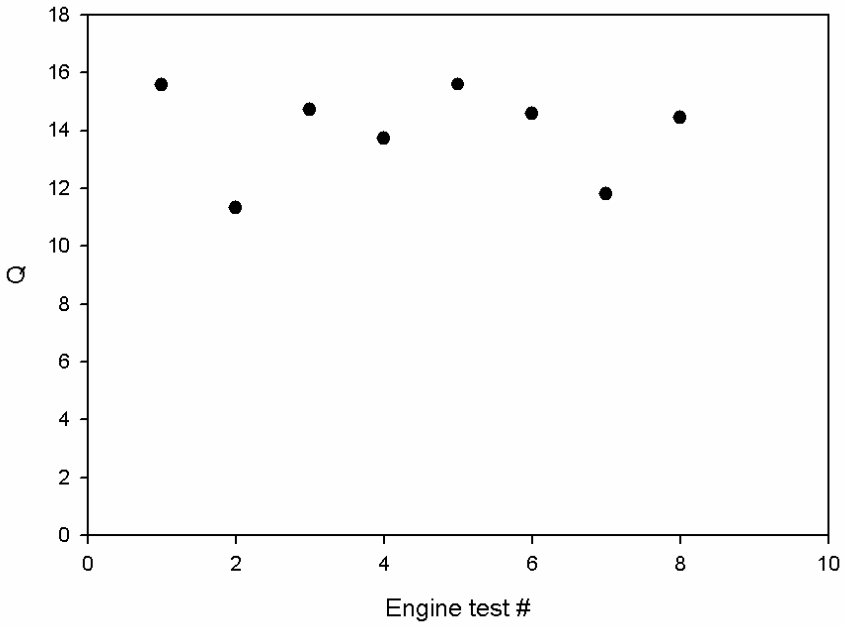


*Figure 28. Q variation for tests with constant parameters.*

The variation of Q between tests with the exact same engine parameters was also considered. All of the engines reported on in Figure 28 have a 3mm bubble, 40um initial deflection and 30V input. As is clear from the previous plots, Q can vary a great deal among engines of the same configuration. The Q data shown in Figure 28 have a mean value of 14.0 with a standard deviation of 1.6. This 11% variation is present in all engine data, and is difficult to control.

### *5.8 ANOVA TRENDS: Q AND PERCENT FRICTION*

Through the statistical analysis detailed in section 4.3, trends were found in the Q data. These trends help to explain which engine parameters affect energy losses the most. The ANOVA analysis showed that the following trends were present in the parametric study: Q does not vary with input voltage or initial deflection, but Q does vary with

cavity thickness and bubble size. This analysis reveals whether the means are different, but not which way the trend goes. Trends were determined by examination of the data sets and their respective means. It was found that a larger cavity thickness yielded a higher Q value, and a smaller bubble size also yielded a higher Q value. These results raise the question of what exact parameter is causing these trends, in terms of mass, stiffness and damping inside the engine during testing. To examine these parameters further, a linearly coupled oscillator model was utilized, which will be detailed in Chapter 6.

### *5.9 PERCENT FRICTION COMPARISON*

Using the data in Figure 27, the percent friction was calculated. Since %f is calculated directly from Q, the two figures are very similar, with opposite trends due to the inverse relationship between Q and %f.

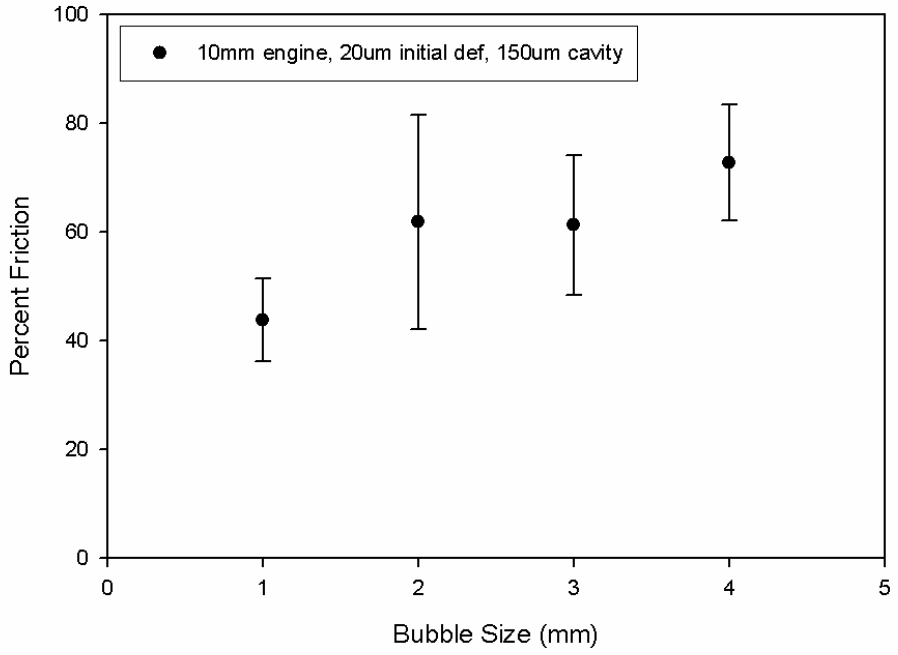


*Figure 29. Percent friction variation with bubble size, same data as Figure 27.*

These percent friction values can be compared to the mechanical efficiency of large-scale engines, presented in section 1.3.3. Reported mechanical efficiencies of internal combustion engines vary from 55-90% [21], which can be indirectly compared with the values of percent friction in Figure 29. A comparison can be made by subtracting the reported mechanical efficiencies from 100, and comparing this value with the percent friction. This energy lost yields values of 10-45%, which is slightly lower than the calculated percent friction of the P3 engine, as in Figure 29, of 40-70%. This means that the friction or energy lost in the P3 engine during operation can be very similar to the friction in large scale engines, which is not the case for other micro engines, as reported in section 1.3.1.

# CHAPTER SIX
# ENGINE MODELING

A linearly-coupled oscillator model of the engine was developed to be able to change individual engine parameters and examine the effect on energy losses in the engine. This model also enables engine optimization.

## *6.1 ELECTRICAL-MECHANICAL ANALOGY*

As a first attempt at modeling, the electrical-mechanical analogy was used to create an RLC circuit to approximate the mass-spring-damper system of the engine [55-57]. In this analogy, an electrical circuit can approximate a mechanical system because they both follow the same differential equation. Table 8 shows how the components are correlated in the analogy.

*Table 8. Electrical-mechanical correlation using force-voltage analogy. [25]*

| Mechanical Systems | Electrical Systems |
|---|---|
| Force | Voltage |
| Mass | Inductance |
| Viscous-friction coefficient | Resistance |
| Spring constant | Reciprocal of capacitance |
| Displacement | Charge |
| Velocity | Current |

Using the circuit simulation software "PSpice", an RLC circuit was constructed to approximate the mass-spring-damper system of the engine. The mechanical system described required three springs in series which represent the stiffnesses of the upper membrane, liquid, and lower membrane. However, the program PSpice did not allow more than one capacitor in series. Therefore, the program would not allow a physically accurate description of the mechanical system, so other software simulation methods were sought.

## *6.2 WORKING MODEL*

A linearly coupled oscillator model was created using a program called "Working Model." Working Model [58] is a 2D simulation program that allows simulation of collisions, mass-spring-damper systems and other dynamic mechanical systems. The model was created to physically simulate the engine as a system of two mass-spring-damper systems in series. Therefore, the upper membrane was modeled as a mass anchored by a spring and damper which had the characteristics of the membrane. To simplify the system, the lower membrane and liquid were combined into one mass-spring-damper system connected to the upper membrane. This approximation should be fairly good for actual engine operation, as it is assumed that the mass of liquid in the cavity dominates the mass of the lower membrane.

A time-dependent force is approximated based on experimental data and is applied on the upper membrane. In experiments, a heat pulse is applied to the heater for 200μsec, so in the model, the force in the y-direction is applied to the upper membrane for 200μsec. The amplitude of the force applied in the model is defined by matching the model deflection amplitude with experimental deflection data.

### *6.2.1 Working Model Generator Model*

In order to verify the characteristics of the program, a model of a membrane generator was created. This model is simpler than the engine, as it is only one mass-spring-damper system, shown in Figure 30. Experimental and calculated values were used for the generator model parameters, and the output of the program was compared to experimental data. Using the physical constants and values, it was found that the model matched the experimental resonance, Q, peak deflection and peak velocity when the parameters were set to the values in Table 9.

*Table 9. 5mm generator parameter values.*

| | Experimental: | Model: |
|---|---|---|
| Stiffness (N/m): | 3100 | 620 |
| Mass (kg): | 5.5e-7 | 5.64e-7 |
| Damping (Ns/m): | -- | 2.66e-4 |
| Resonance (Hz): | 5270 | 5276 |
| Q: | 70 | 70 |

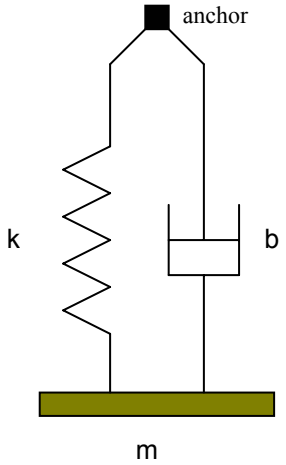


*Figure 30. Diagram of generator model.*

### *6.2.2 Working Model Engine Model*

As an approximation, the engine model was defined as two mass-spring-damper systems in series. The model parameters were defined to match experimental data of a 6mm generator on an engine. These parameters and their values are listed in Table 10. The values of these parameters were either matched from experimental data (membrane stiffnesses), calculated from physical characteristics (mass), or experimental ringout data (damping ratios). Since the simple model was verified with a generator, this engine model was verified with a generator as the upper membrane as well. The liquid stiffness was approximated by the surface tension of the water-air interface [16]. A diagram of this engine model is shown in Figure 31.

*Table 10. 6mm generator on engine model parameter values.*

| Parameter: | Relationship: | Value: |
|---|---|---|
| Upper membrane damping (Ns/m) | Linear | 3e-5 |
| Upper membrane stiffness (N/m) | Linear | 70 |
| Upper membrane mass (kg) | Constant | 7.95e-7 |
| Liquid damping (Ns/m) | Linear | 3e-4 |
| Liquid stiffness (N/m) | Linear | 0.073 |
| Liquid mass (kg) | Constant | 3.6e-6 |

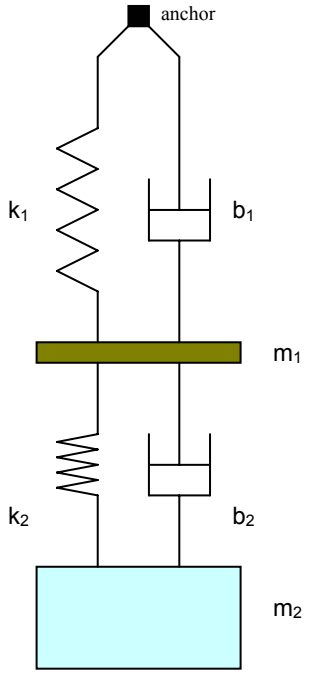


*Figure 31. Diagram of engine model.*

### *6.3 MODEL RESULTS*

The engine model in Figure 31 was used to determine which engine parameters (governing equation parameters) have the largest effect on resonance and Q. This will allow us to correlate the engine configuration parameters (bubble size, initial deflection, cavity thickness, membrane size) with the governing equation system parameters (mass, stiffness, damping). The complexity of the system enters because of the interconnected nature of these parameters.

The engine model was first verified with experimental data. Figure 32 shows the comparison between the model ringout and an experimental ringout of an engine with a 6mm generator.

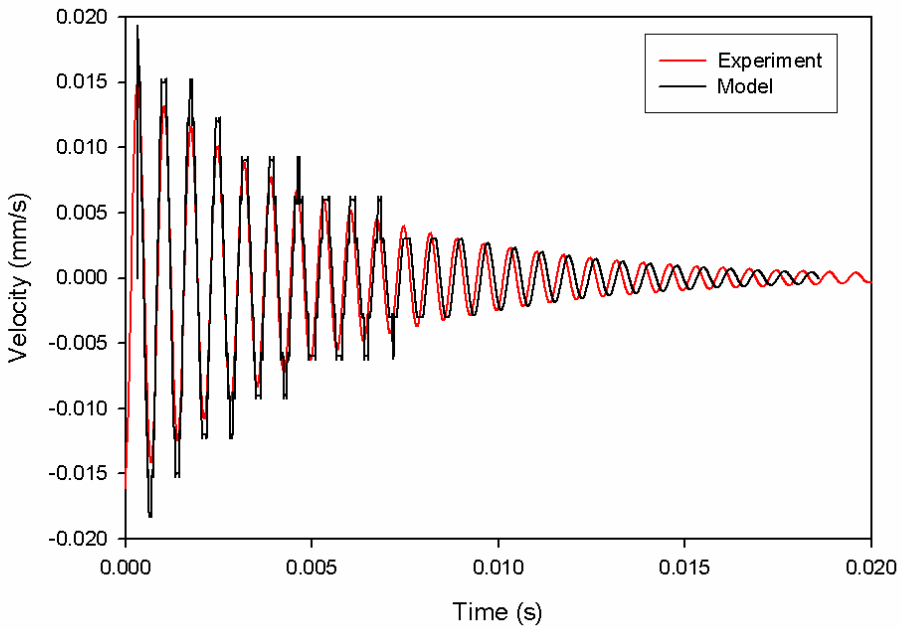


*Figure 32. Comparison between experiment and model for 6mm generator engine.*

Next, a study was conducted using the model parameter values to determine which has the greatest effect on engine resonance and Q. The stiffness of the generator was varied from model values of 5 to 700 N/m. The results shown in Figure 33 correlate well with the theoretical equation, which defines a trend of stiffness raised to the ½ power for both resonance and Q.

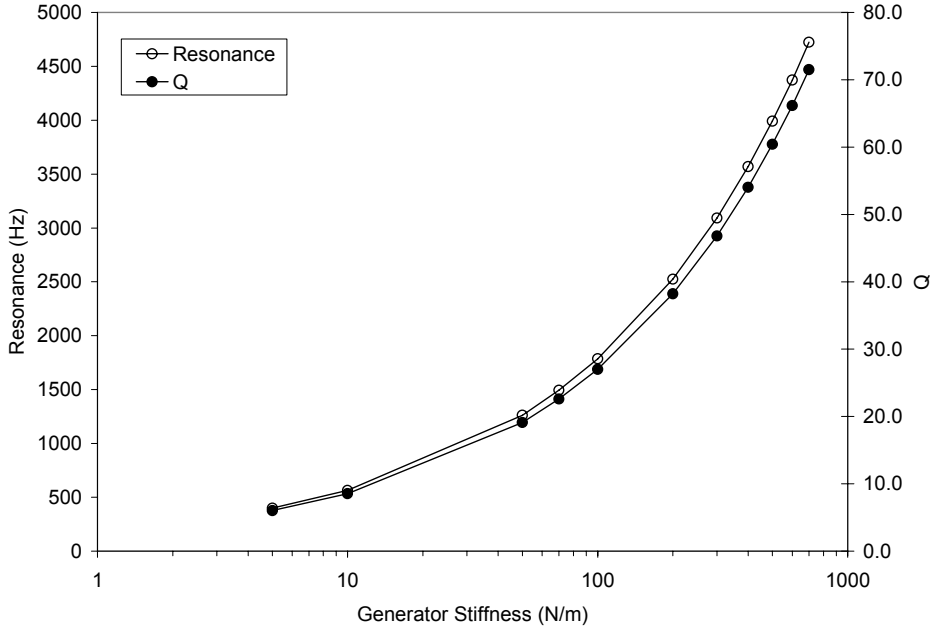


*Figure 33. Varying model generator stiffness keeping all other variables constant.*

The model matches experimental results at a generator stiffness value of 70 N/m. Resonance and Q increase if the generator stiffness is increased, following the appropriate trend.

Figure 34 shows the dependence of resonance and Q on the stiffness of the liquid. The generator stiffness was set to the experimentally-verified model value of 70 N/m. All other parameters were held constant. The surface tension of the water-air interface was used to approximate the stiffness of the liquid, and is 0.073 N/m. Increasing the generator stiffness has a greater effect than increasing the liquid stiffness. As can be seen in the upper portions of Figure 33 and Figure 34, if the generator stiffness is increased by a factor of 10, resonance is about 4700Hz, with a Q of 70; whereas if the stiffness of the liquid was increased by a factor of 100, resonance is about 1570Hz with a Q of 23.

These results show that the generator stiffness should be used to tailor the resonance and Q of the engine rather than changing the liquid stiffness. For example,

increasing the generator stiffness by a factor of 10 yields a 68% increase in resonance and Q, while increasing the liquid stiffness by a factor of 10 yields only a 0.5% increase in resonance and Q.

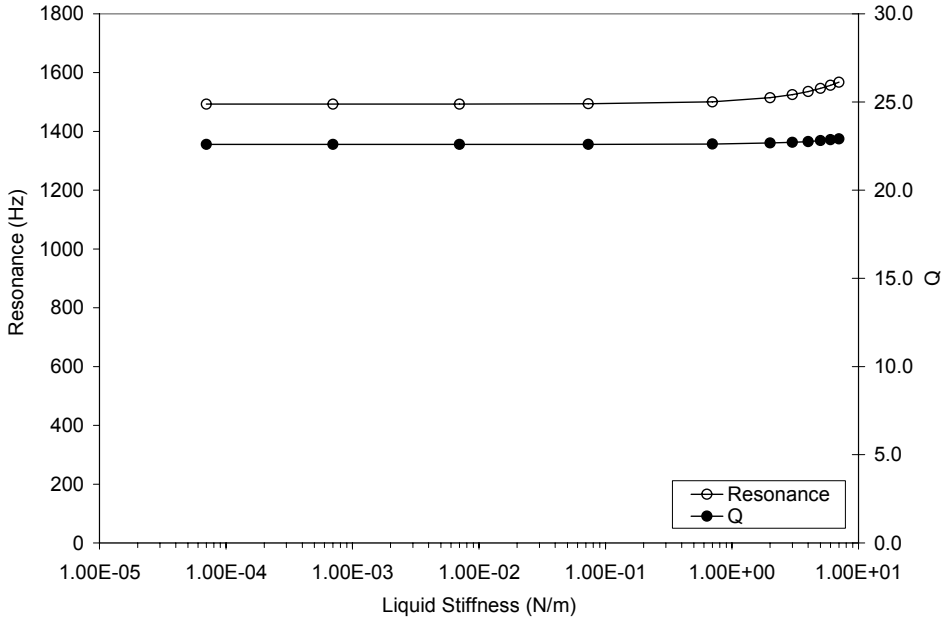


*Figure 34. Varying model liquid stiffness keeping all other variables constant.*

The effect of the mass of liquid was also studied in the model. The model value of the mass of the liquid was varied from 4e-7 kg to 3e-3 kg, and the results are shown in Figure 35. It is clear that there is no dependence on resonance and Q for this range of mass values. The actual calculated mass in the engine experimentally is given in Table 10, so this range of values encompasses what could be achieved in reality.

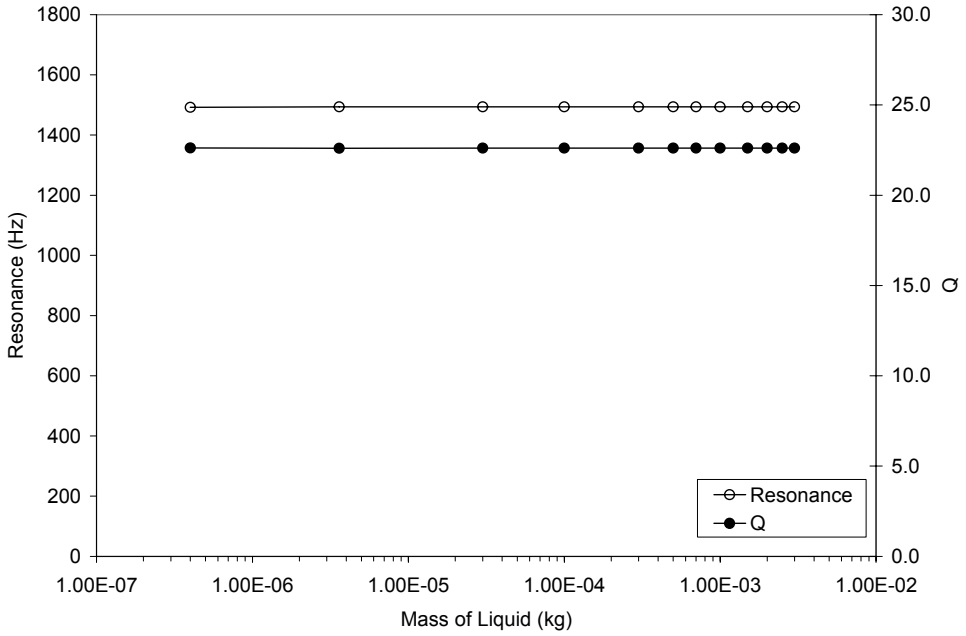


*Figure 35. Varying model liquid mass keeping all other variables constant.*

The trend seen here sheds light on the experimental trend found in section 5.7 of decreasing Q with increasing bubble size in the engine. This suggests that the dominant factors are the damping/stiffness and not the mass, and also that a larger bubble produces more damping/less stiffness.

This result also agrees well with the theoretical expressions for resonance and Q, given in Equations (10) and (11), where the mass is raised to the ½ power. Since the mass is such a small number, unless large changes are seen, it has little effect on resonance and Q of the engine.

### *6.4 MODEL PARAMETRIC STUDY*

A parametric study was undertaken with a 10mm engine model to verify the trends seen in section 5.7. The structure of the model is the same as in Figure 31, but the parameter values and geometry were changed to represent a 10mm bare Si upper membrane and 6mm heater. These values are given in Table 11.

*Table 11. 10mm engine model parameter values.*

| Parameter: | Relationship: | Value: |
|---|---|---|
| Upper membrane damping (Ns/m) | Linear | 1e-5 |
| Upper membrane stiffness (N/m) | Linear | 4 |
| Upper membrane mass (kg) | Constant | 4.66e-7 |
| Liquid damping (Ns/m) | Linear | 1e-4 |
| Liquid stiffness (N/m) | Linear | 0.073 |
| Liquid mass (kg) | Constant | 7.5e-6 |

It was assumed that the stiffness of the upper membrane for an initial deflection of 20μm was half that of an initial deflection of 40μm. This is a good assumption because the springs in the model are linear. Using this relationship, the stiffness of the upper membrane was varied to simulate changes in initial deflection, and the resulting effect on Q was observed. The same trend shown in Figure 26 was seen with the model, and similar Q values were obtained. Table 12 shows the comparison between initial deflection values and model stiffness values, along with the corresponding value or range of values of Q.

*Table 12. 10mm engine model initial deflection parametric study values.*

| Initial Deflection (μm): | Q (experimental): | Model Stiffness (N/m): | Q (model): |
|---|---|---|---|
| 20 | 7-15 | 4 | 12.4 |
| 25 | 9-15 | 4.8 | 13.6 |
| 30 | 11-16 | 6 | 15.2 |

The same technique was used to verify the trend of Q with bubble size reported in section 5.7. Mass was not shown to be dominant in the previous section, and so it was assumed that the change in bubble size affected the stiffness of the liquid. Proportional changes in the liquid stiffness corresponding to changes in bubble size were applied to the model, but the results showed no change in Q. Therefore, the assumption that stiffness was the dominant parameter was incorrect. Damping was shown to dominate for

changes in bubble size over mass and stiffness. The same study was performed using changes in the damping of the liquid, and the trend seen earlier was confirmed. The values are given in Table 13.

*Table 13. 10mm engine bubble size parametric study values.*

| Bubble Size (mm): | Q (experimental): | Model Damping (Ns/m): | Q (model): |
|---|---|---|---|
| 1 | 12-17 | 5e-5 | 22.8 |
| 2 | 7-15 | 1e-4 | 12.4 |
| 3 | 7-12 | 1.5e-4 | 8.5 |
| 4 | 7-11 | 2e-4 | 6.5 |

The 10mm experimental data used to verify the model were an engine with a 2mm bubble, which is why that configuration matches the experimental data. The average experimental value of Q for this configuration was used to calibrate the model. It can be seen in Table 13 that the model overestimated Q for the smaller bubble sizes, but the trend shown matches experimental results. Increasing the bubble size and increasing the damping show the same trend. This result is supported by literature [59] where it was shown that larger air bubbles in water have higher damping.

### *6.5 MODEL RESULTS SUMMARY*

These results show which engine parameters are dominating the system behavior, which was the stated goal of this study. Here the membrane stiffness (initial deflection) and liquid damping (bubble size) are the dominant parameters. This result can lead to optimization of the engine, focusing on these two values out of the many engine parameters. Overall, the model showed that higher initial deflections (upper membrane stiffness) and smaller bubble sizes (liquid damping) yield less energy lost per cycle (higher Q).

If a single engine parameter was chosen that dominates the system, it would be the liquid damping. The experimental parametric study of initial deflection in Figure 26 showed no statistically significant trend with Q, and indeed the model showed smaller (20%) changes in Q for changes in initial deflection. Therefore, the liquid damping should be tailored to produce the greatest changes in Q.

Membrane stiffness trends can also be applied to the size and material of the membrane, not just the initial deflection. Any configuration and properties of the upper membrane that yield a stiffer response will also yield a higher Q and resonant frequency. However, changing the size of the upper membrane also changes the size of the cavity, which will change the liquid damping. Controlling liquid damping is more difficult to implement, but the model shows this is the parameter that dominates the system, not the liquid mass or stiffness. The model has shown that the two parameters to focus on for engine optimization are the upper membrane stiffness and the liquid damping.

# CHAPTER SEVEN
# CONCLUSIONS

The P3 engine operates as a complex system of interacting mass-spring-damper systems. Parametric experimental studies have shown how the behavior changes when the key components of the system are changed. A linearly coupled oscillator model has developed even more insight into how the system and engine can be optimized.

The relationships between the resonant frequency of the engine, Q, and the various engine parameters have been established. Engine parameters studied include: cavity thickness, initial deflection, bubble size, heat input, and upper membrane size. Engine performance was studied using a free vibration (ringout) response. These studies have shown that heat pulses and mechanical impacts yield similar engine outputs, the atmospheric pressure around the engine affects this response, and the size of the upper membrane did not show a clear trend with Q. A parametric study of the 10mm engine showed how each parameter affected Q, with the largest effect originating from the bubble size in the engine, which was shown to be representative of the liquid damping.

A linearly coupled oscillator model was used to show how each of these parameters is decomposed into the governing equation coefficients. Parametric studies and modeling have shown that the single most dominant parameter in the engine configuration is the liquid damping. Increasing the upper membrane stiffness, liquid stiffness, and liquid mass by a factor of 10 yields 68%, 0.5% and 0.01% increases in Q, respectively. Increases in liquid damping showed the same trend as increases in bubble size. This relationship is the key to optimizing the energy losses in the engine. An engine

with a 1mm bubble achieved a Q value of 22.8 according to the model, whereas an engine with a 4mm bubble only reached a Q of 6.5.

The next most influential parameter is the upper membrane stiffness. Resonance and Q increase with increasing upper membrane stiffness. Several methods can be used to increase the stiffness of the upper membrane, including the initial deflection, the membrane material, the membrane geometry and size. A target resonant frequency should be used to tailor the engine parameters to try to achieve the lowest possible losses in the engine to assure efficient operation.

## REFERENCES

[1] Cho, J., Wiser, T., Richards, C., Bahr, D., Richards, R., "Fabrication and characterization of a thermal switch", Sensors and Actuators A, in press, 2006

[2] Hsu, T-R., MEMS & Microsystems: Design and Manufacture, McGraw-Hill, New York, NY, p. 216-217, 221-225, 2002

[3] Xinli, W., Shumei, C., Shukang, C., "Advantages of Electrostatic Micromotor and Its Application to Medical Instruments", Conference Record—IEEE Industry Applications Society Annual Meeting, v. 4, p. 2466-2468, 2002

[4] Suzuki, K., Tanigawa, H., "Single Crystal Silicon Rotational Micromotors", Proceedings of IEEE Micro Electro Mechanical Systems, p. 15-20, 1991

[5] Epstein, A.H., Senturia, S.D., Anathasuresh, G., Ayon, A., Breuer, K., Chen, K-S, Ehrich, F.E., Gauba, G., Ghodssi, R., Groshenry, C., Jacobson, S., Lang, J.H., Lin, C-C, Mehra, A., Miranda, J.M., Nagle, S., Orr, D.J., Piekos, E., Schmidt, M.A., Shirley, G., Spearing, M.S., Tan, C.S., Tzeng, Y-S, Waitz, I.A., "Power MEMS and Microengines", 1997 International Conference on Solid-State Sensors and Actuators, Chicago, IL, June 16-19, 1997

[6] Khanna, R., "MEMS fabrication perspectives from the MIT Microengine Project", Surface and Coatings Technology, v. 163-164, p. 273-280, 2003

[7] Lee, D.H., Park, D-E, Yoon, E., Kwon, S., "A MEMS Piston-Cylinder Device Actuated by Combustion", Journal of Heat Transfer, v. 125, 2003

[8] Heywood, J.B., Internal Combustion Engine Fundamentals, McGraw-Hill, New York, NY, p. 24, 81, 196, 712, 713, 714, 725, 726, 1988

[9] Lee, C.H., Jiang, K.C., Jin, P., Prewett, P.D., "Design and fabrication of a micro Wankel engine using MEMS technology", Microelectronic Engineering, v. 73-73, p. 529-534, 2004

[10] Smith, N.F., Tanner, D.M., Swanson, S.E., Miller, S.L., "Non-Destructive Resonant Frequency Measurement on MEMS Actuators", IEEE 39th Annual International Reliability Physics Symposium, Orlando, FL, 2001

[11] Whalen, S., Cycle Work from a MEMS Heat Engine and Characterization of the Liquid-Vapor Phase Change Actuation Mechanism, PhD Dissertation, WSU, Department of Mechanical Engineering, p. 117, 2004

[12] Lumley, J.L., Engines: An Introduction, Cambridge University Press, Cambridge, UK, p. 123, 1999

[13] Stone, R., Introduction to Internal Combustion Engines, Macmillan, London, p. 233, 1985

[14] Harman, R.T.C., Gas Turbine Engineering: Applications, Cycles and Characteristics, Wiley & Sons, New York, NY, p. 39, 214, 1981

[15] Mehrtens, A.C., Gas Engine Theory and Design, Wiley & Sons, New York, NY, p. 33, 69, 1909

[16] Crowe, C.T., Elger, D.F., Roberson, J.A., Engineering Fluid Mechanics, Seventh Edition, Wiley & Sons, New York, NY, p. 24, 279, 2001

[17] Duwel, A., Gorman, J., Weinstein, M., Borenstein, J., Ward, P., "Experimental study of thermoelastic damping in MEMS gyros", Sensors and Actuators A, v. 103, p. 70-75, 2003

[18] Peters, R.D., "Model of Internal Friction Damping in Solids", http://arxiv.org/html/physics/0210121, 2002

[19] Quy, T.A., Carpenter, D.A., Richards, C.D., Bahr, D.F., Richards, R.F., "Evaporative Heat Transfer from Ten-Micron Micro-Channels", Proceedings of 2005 ASME International Mechanical Engineering Congress and Exposition, November 5-11, Orlando, FL, 2005

[20] Cengel, Y., Boles, M., Thermodynamics: An Engineering Approach, Third Edition, McGraw-Hill, New York, NY, p. 256, 1998

[21] Obert, E.F., Internal Combustion Engines and Air Pollution, HarperCollins, New York, NY, p. 43, 44, 481, 482, 1973

[22] Allen, J.R., Bursley J.A. Heat Engines: Steam, Gas, Steam Turbines and Their Auxiliaries McGraw-Hill, New York, NY, p. 302, 1931

[23] Obert, E.F., Internal Combustion Engines: Analysis and Practice, Second Edition, International Textbook Co., Scranton, PA, p. 38, 432, 1950

[24] Hamilton, E.H., Elementary Thermodynamics of Automobile Engines, First Edition, McGraw-Hill, New York, NY, p. 229, 1923

[25] Ogata, K., System Dynamics, Third Edition, Prentice Hall, Saddle River, NJ, p. 158, 248, 1998

[26] Torndahl, M., Almqvist, M., Wallman, L., Persson, H.W., Lindstrom, K., "Characterisation and comparison of a cMUT versus a piezoelectric transducer for air applications", 2002 IEEE Ultrasonics Symposium, 2002

[27] Caliano, G., Savoia, A., Caronti, A., Foglietti, V., Cianci, E., Pappalardo, M., "Capacitive micromachined ultrasonic transducer with an open-cells structure", Sensors and Actuators A, v. 121, p. 382-387, 2005

[28] Caronti, A., Caliano, G., Iula, A., Pappalardo, M., "An Accurate Model for Capacitive Micromachined Ultrasonic Transducers", IEEE Transactions on Ultrasonics, Ferroelectrics, and Frequency Control, v. 49, n. 2, 2002

[29] McIntosh, J.S., Hutchins, D.A., Billson, D.R., Robertson, T.J., Noble, R.A., Jones, A.D.R., "The characterization of capacitive micromachined ultrasonic transducers in air", Ultrasonics, v. 40, p. 477-483, 2002

[30] McIntosh, J.S., Hutchins, D.A., Billson, D.R., Noble, R.A., Davies, R.R., Koker, L., "SAFT Imaging Using Immersed Capacitive Micromachined Ultrasonic Transducers", 2002 IEEE Ultrasonics Symposium, 2002

[31] Jin, X., Ladabaum, I., Degertekin, F.L., Calmes, S., Khuri-Yakub, B.T., "Fabrication and Characterization of Surface Micromachined Capacitive Ultrasonic Immersion Transducers", IEEE Journal of Microelectromechanical Systems, v. 8, n. 1, 1999

[32] Noble, R.A., Bozeat, R.J., Robertson, T.J., Billson, D.R., Hutchins, D.A., "Novel Silicon Nitride Micromachined Wide Bandwidth Ultrasonic Transducers", 1998 IEEE Ultrasonics Symposium, 1998

[33] Baborowski, J., Ledermann, N., Muralt, P., "Piezoelectric Micromachined Transducers (PMUT's) Based on PZT Thin Films", 2002 IEEE Ultrasonics Symposium, 2002

[34] Percin, G., Khuri-Yakub, B.T., "Piezoelectrically Actuated Flextensional Micromachined Ultrasound Transducers—II: Fabrication and Experiments", IEEE Transactions on Ultrasonics, Ferroelectrics, and Frequency Control, v. 49, n. 5, 2002

[35] San Emeterio, J.L., "Determination of Electromechanical Coupling Factors of Low Q Piezoelectric Resonators Operating in Stiffened Modes", IEEE Transactions on Ultrasonics, Ferroelectrics, and Frequency Control, v. 44, n. 1, 1997

[36] Sasaki, Y., Takahashi, S., Yamamoto, M., "Mechanical Quality Factor of Multilayer Piezoelectric Ceramic Transducers", Japanese Journal of Applied Physics, v. 40, p. 3549-3551, 2001

[37] Muralt, P., Baborowski, J., "Micromachined Ultrasonic Transducers and Acoustic Sensors Based on Piezoelectric Thin Films", Journal of Electroceramics, v. 12, p. 101-108, 2004

[38] Paul, O., Baltes, H., "Mechanical behavior and sound generation efficiency of prestressed, elastically clamped and thermomechanically driven thin film sandwiches", Journal of Micromechanics and Microengineering, v. 9, 1999, p. 19-29

[39] Prak, A., Blom, F.R., Elwenspoek, M., Lammerink, T.S.J., "Q-Factor and Frequency Shift of Resonating Silicon Diaphragms in Air", Sensors and Actuators A, v. 25-27, p. 691-698, 1991

[40] Nayfeh, A.H., Younis, M.I., "A new approach to the modeling and simulation of flexible microstructures under the effect of squeeze-film damping", Journal of Micromechanics and Microengineering, v. 14, p. 170-181, 2004

[41] Stemme, E., Stemme, G., "A Balanced Dual-Diaphragm Resonant Pressure Sensor in Silicon", IEEE Transactions on Electron Devices, v. 37, n. 3, 1990

[42] Humphris, A.D.L., Tamayo, J., Miles, M.J., "Active Quality Factor Control in Liquids for Force Spectroscopy" Langmuir, v. 16, p. 7891-7894, 2000

[43] Bergaud, C., Nicu, L., "Viscosity measurements based on experimental investigations of composite cantilever beam eigenfrequencies in viscous media", Review of Scientific Instruments, v. 71, n. 6, 2000

[44] Brand, O., Lenggenhager, R., Baltes, H., "Influence of Air Pressure on Resonating and Thermoelectric Microstructures Realized with Standard IC Technologies", International Electron Devices Meeting, 1993

[45] Cho, J., Anderson, M., Richars, R., Bahr, D., Richards, C., "Optimization of electromechanical coupling for a thin-film PZT membrane: I. Modeling", Journal of Micromechanics and Microengineering, v. 15, p. 1797-1803, 2005

[46] Buser, R.A., De Rooij, N.F., "Resonant Silicon Structures", Sensors and Actuators, v. 17, p. 145-154, 1989

[47] Lucklum, R., Schranz, S., Behling, C., Eichelbaum, F., Hauptmann, P., "Analysis of compressional-wave influence on thickness-shear-mode resonators in liquids", Sensors and Actuators A, v. 60, p. 40-48, 1997

[48] Timoshenko, S., Lessells, J.M., Applied Elasticity, First Edition, Westinghouse, East Pittsburgh, PA, p. 261, 313, 1925

[49] Gifford, R., Resonant Frequency Characterization of a Novel MEMS Based Membrane Engine, M.S. Thesis, WSU, Department of Mechanical Engineering, p. 31, 53-66; 2004

[50] Vibrometer Controller User Manual OFV-500, p. 5-9, Polytec GmbH, Waldbronn, Germany manufactured Dec. 2003

[51] SigmaPlot 9.0 User's Manual, Systat Software, Inc., 2004

[52] IEEE Standard on Piezoelectricity, IEEE Std 176, p. 38-52, 1987

[53] Brand, O., Lenggenhager, R., Baltes, H., "Influence of Air Pressure on Resonating and Thermoelectric Microstructures Realized with Standard IC Technologies," IEEE Electron Devices Meeting, p. 195-198, 5-8 Dec 1993

[54] Mertens, J., Finot, E., Thundat, T., Fabre, A., Nadal, M.H., Eyraud, V., Bourillot, E., "Effects of temperature and pressure on microcantilever resonance response", Ultramicroscopy, v. 97, p. 119-126, 2003

[55] Gerber, E.A., Ballato, A., Eds., Precision Frequency Control, Volume 1: Acoustic Resonators and Filters, Academic Press, Inc., p. 103, 1985

[56] Kim, J.S., Choi, K., Yu, I., "A New Method of Determining the Equivalent Circuit Parameters of Piezoelectric Resonators and Analysis of the Piezoelectric Loading Effect", IEEE Transactions on Ultrasonics, Ferroelectrics, and Frequency Control, v. 40, n. 4, p. 424-426, 1993

[57] Xu, C.H., Hu, J.H., Chan, H.L.W., "Behavior of a PZT ring under non-uniform mechanical stress", Ultrasonics, v. 39, p. 735-742, 2002

[58] Working Model User's Manual, Version 5.0, MSC.Software Corporation, 2000

[59] Eller, A.I., "Damping Constants of Pulsating Bubbles", Journal of the Acoustical Society of America, Letters to the Editor, v. 47, n. 5, part 2, p. 1469-1470, 1970

# APPENDIX A

## DETAILED MICROFABRICATION STEPS

Oxide Patterning:

1. Clean wafer with five step process: Acetone, IPA, DI, Acetone, IPA, canned air.
2. Spin on HMDS: cover ¼ of wafer surface and spin at 3000rpm for 30sec.
3. Spin on AZ5214: cover ¾ of wafer surface and spin at 3000rpm for 30sec.
4. Bake wafer at 110ºC for 1min.
5. Align mask with wafer on mask aligner and bring into contact.
6. Expose with UV for 16sec.
7. Develop wafer in solution of 4:1 developer and DI for 1min.
8. Rinse with DI.
9. Cover boron side of wafer with semiconductor tape. Make sure tape edges are pressed firmly with no air pockets.
10. Etch in BOE (10:1) for 5min.
11. Clean wafer in spin-rinse dryer: 60sec rinse, 90sec rinse, 60sec spin/dry.
12. Remove semiconductor tape.
13. Clean wafer with five step process.

Silicon Etch - EDP:

1. Place wafer into pyrex wafer carrier.
2. Dip wafer into EDP bath. EDP temperature should be around 100ºC.
3. Etch for 6 hours.
4. Rinse six times with DI water before removing wafer from pyrex carrier.
5. Clean wafer with five step process.

Gold Patterning:

1. Clean wafer with five step process.
2. Spin on HMDS: cover ¼ of wafer surface and spin at 3000rpm for 30sec.
3. Spin on AZ5214: cover ¾ of wafer surface and spin at 3000rpm for 30sec.
4. Bake wafer at 110ºC for 1min.
5. Align mask with wafer on mask aligner and bring into contact.
6. Expose with UV for 16sec.
7. Develop wafer in solution of 4:1 developer and DI for 1min.
8. Rinse with DI.
9. Etch in gold etchant. Time duration varies with strength of solution. May take as little as 20sec to etch all the exposed gold.
10. Rinse in DI.
11. Etch in hydrogen peroxide to remove TiW layer for 40sec.
12. Rinse in DI.
13. Clean wafer with five step process.
14. Test resistance of each heater for shorting. Resistance should be between 70-300Ω depending on the pattern.

## APPENDIX B

## DETAILED WORKING MODEL SETTINGS

Global:

- Accuracy: Custom – 1e-5 sec, 15 significant digits
- No Gravity
- No Air Resistance
- Electrostatics OFF
- Force Field OFF

Generator Model:

- m = 5.64e-7 kg
- k = 620 N/m
- b = 2.66e-4 Ns/m

6mm Generator on Engine Model:

- $m_1$ = 7.95e-7 kg
- $m_2$ = 3e-6 kg
- $k_1$ = 70 N/m
- $k_2$ = 0.073 N/m
- $b_1$ = 3e-5 Ns/m
- $b_2$ = 3e-4 Ns/m

10mm Engine Model:

- $m_1$ = 4.66e-7 kg
- $m_2$ = 7.5e-6 kg
- $k_1$ = 4 N/m
- $k_2$ = 0.073 N/m
- $b_1$ = 1e-5 Ns/m
- $b_2$ = 1e-4 Ns/m